Title

Capturing Fluctuation Dynamics In BaTiO3 Ferroelectric Domains Through X-ray Photon Correlation Spectroscopy

Author

Rao, Pooja

Publication Date

2024

Peer reviewed|Thesis/dissertation

Capturing Fluctuation Dynamics In $BaTiO_3$ Ferroelectric Domains Through X-ray Photon Correlation Spectroscopy

By

POOJA RAO
THESIS

Submitted in partial satisfaction of the requirements for the degree of

MASTER OF SCIENCE

in

Materials Science and Engineering

in the

OFFICE OF GRADUATE STUDIES

of the

UNIVERSITY OF CALIFORNIA

DAVIS

Approved:

Roopali Kukreja, Chair

Yayoi Takamura

Seung Sae Hong

Committee in Charge

2024

To my grandfather, K. N. Srikanta Murthy,
whose love and support served as an inspiration.

Abstract

Temporal fluctuations in functional materials are critical for both phase stability and transformation processes. In these materials, nanoscale fluctuations play a pivotal role in mesoscale phenomena, such as domain reorientation and domain wall nucleation. Investigating the dynamics of these fluctuations is essential for a fundamental understanding of the landscape of domains and for enhancing the ability to tune and stabilize them for technical applications. In this thesis, I focus on the transformation of ferroelectric domains in $BaTiO_3$ by examining the fluctuations of in-plane (*a*/*b*) domains. To probe the relevant spatial and temporal scales necessary for studying fluctuation dynamics, I employed a synchrotron-based coherent scattering technique known as x-ray photon correlation spectroscopy (XPCS). The primary objective of this research was to compare dynamic fluctuations among different types of domains during phase transitions, complementing existing studies on other domain configurations in $BaTiO_3$. The XPCS results revealed that *a*/*b* domain fluctuations accelerate as phase transitions approach, a behavior also observed in *a*/*c* domains. Furthermore, this thesis explores the *q*-dependence of fluctuation behavior. I first examined whether similar fluctuation trends occurred across different orders of domain scattering peaks and also investigated potential q-dependence of fluctuations within a single peak. Analyzing various regions of *q*-space offers deeper insights into different aspects of domain configuration, such as domain walls. This investigation into the dynamic behavior of ferroelectric domains contributes to our understanding of the driving forces behind domain transformations and aids in optimizing the switching and stability of domains.

Acknowledgements

First, I would like to thank Professor Roopali Kukreja for being an incredible advisor and guide. She has supported me through all my ups and downs and always encouraged me to be the best researcher I can. I have grown tremendously throughout my time working with Professor Kukreja and I am extremely grateful for every experience.

Next, I would like to thank my committee – Professor Yayoi Takamura and Professor Seung Sae Hong for their support throughout my degree and in this thesis. I'd additionally like to thank all the faculty whose courses have provided me with the tools to complete this degree.

The research in this thesis could not have been done without the support of our collaborators. I would like to thank Dr. A. S. Everhardt and Dr. S. Matzen in Dr. B. Noheda's group at the University of Groningen for their support in sample fabrication. Additionally, I would like to thank Andrei Fluerasu and Xiaoqian Chen at the CHX beamline in NSLS-II for their guidance in beamtimes. None of the work in this thesis could have been done without these people.

I want to thank all my colleagues from the Kukreja group – Jugal, Meera, Rahul, Jianheng, Yu Hsing, Cun Shuo, Scott, Surya, Nushrat, Emma, Nanna, Ankit and Jesse for making our lab such a supportive and fun place.

I would like to thank my best friends who I would be nowhere without – Steph, Yaniel, Hannah, Julia, and Rajee. I would also like to thank my support system in Davis that have carried me through the last two years – Meera, Rahul, Ido, Jacob, Cun Shuo, and John.

Finally, and most importantly, I would like to thank my family. My father, Chandrashekhar Rao, inspired me to pursue this degree. My mother, Latha Chandrashekhar, for believing in me every

day. And my sister and brother-in-law, Megha Chandrashekhar and Mac Lee, for always being there for me.

Contents

Chapter 1: Introduction

Ferroelectric materials are a class of functional materials which retain spontaneous polarization without the application of an external field or stress [1]. Due to their ability to stably retain and switch polarization, some common applications of ferroelectric materials include nonvolatile memory storage, capacitors, sensors, actuators, etc. Thin film ferroelectric materials are also commonly used as one of their interesting advantages is the formation of ferroelectric domains. Manipulating ferroelectric domains enable applications for energy efficient computing by decreasing power consumption, increasing speed of switching, and increasing information density [2].

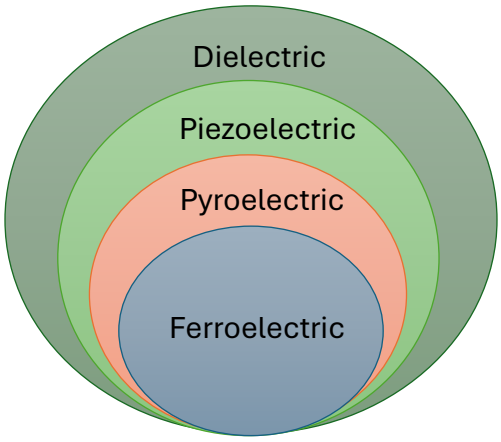

Figure 1.1: Visual representation of ferroelectric materials as a subclass of dielectrics.

Ferroelectric materials are a subset of dielectric materials, as shown below in Fig. 1.1. Dielectrics are insulating materials which can retain dielectric polarization from an applied field due to the creation of temporary electric dipole moments. Some common applications of dielectrics are electronic devices such as capacitors due to their ability to store electrical charge [3]. Within

dielectrics, the next subset of materials is known as *piezoelectric* materials. *Piezoelectricity* is ascribed to the phenomenon where a coupling between strain and electric field occurs within the material. This effect arises due to the generation of a dipole moment from ions as the crystal is deformed. One of the requirements for a material to be piezoelectric is a lack of a center of symmetry, known as non-centrosymmetric crystal structures. Piezoelectric materials which possess a unique axis of symmetry that can also be switched with an applied electric field are called ferroelectric. Ferroelectric materials with the perovskite crystal structure have gained significant interest in scientific communities. Some examples of common ferroelectric materials consist of oxide ceramics such as $BaTiO_3$, $PbTiO_3$, or $Pb[Zr_xTi_{1-x}]O_3$. Note that ferroelectric behavior exists only for a certain temperature range. Above a certain temperature, known as the Curie temperature (T_C), the material transforms to a higher symmetry with no spontaneous polarization (also known as the *paraelectric* phase).

1.1: Characteristics of ferroelectric materials

Polarization in ferroelectric materials is a result of the displacement of cation and anions which cause, net *polarization* (*P*), which can be calculated using the following equation,

$$P = \varepsilon_0 \chi_e E$$

where ε_0 is the *electric permittivity of the free space*, χ_e is the *electric susceptibility* of the material, and *E* is the applied electric field. Electric susceptibility is closely linked to electric permittivity in the following equation,

$$\chi_e = \varepsilon_r - 1$$

where ε_r is the *relative permittivity* of materials. Permittivity of dielectric materials depends linearly on applied electric field. [2].

In a similar manner to ferromagnets, ferroelectric materials also possess hysteretic behavior but are due to electric dipoles instead of spins. As shown in Fig. 1.2, hysteresis for ferroelectric materials shows path dependent behavior, which is not present for the dielectric or paraelectric cases. The ability for ferroelectrics to reliably switch between two stable states makes it very appealing for applications in non-volatile memory storage [2].

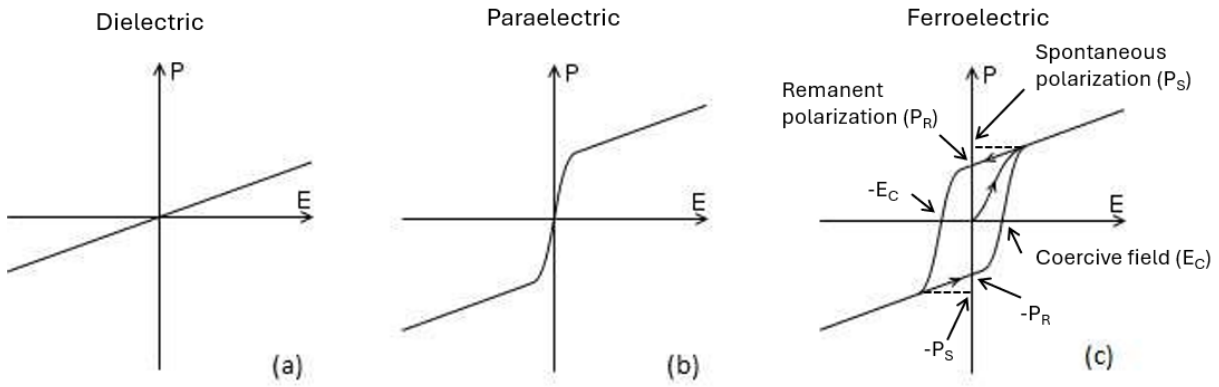

Figure 1.2: Polarization vs E-field: for (a) dielectric, (b) paraelectric, and (c) ferroelectric material with its major components labelled.

As mentioned previously, ferroelectrics are only polar for a certain temperature range, until they reach the T_C, where the material transitions to a paraelectric phase. Above T_C, the permittivity (ε) can be described using the *Curie Weiss law* as described in the equation below,

$$\varepsilon = \frac{C}{(T - T_0)}$$

where C is the *Curie Weiss constant,* and T_0 is the onset of a transition temperature. These transitions can be first-order or second-order based on whether P changes continuously or abruptly with temperature [2].

1.2: Crystal structure and symmetry

Only certain crystal structures which lack a center of symmetry can possess ferroelectricity. One of the most common types of crystal structures that are used for ferroelectric materials are *perovskites*. Perovskites have the general formula of ABX_3 where A and B are cations. For the purposes of this thesis, we will focus on perovskite oxides where the general formula can be rewritten as ABO_3. For the example $SrTiO_3$ in Fig. 1.3, perovskite oxides can be visualized as a Ti cation surrounded by six O^{2-} anions forming a TiO_6 octahedron. The TiO_6 octahedra corner shared in the *x*, *y*, and *z* directions resulting a in perovskite crystal structure. Sr atoms sit in the center of eight TiO_6 octahedra [4]. Some examples of common perovskite oxide materials are $SrTiO_3$, $PbTiO_3$, and $BaTiO_3$.

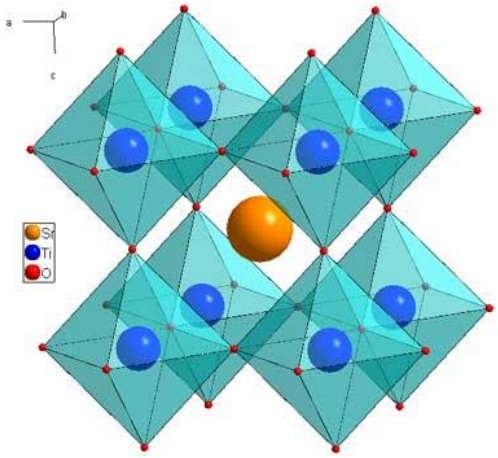

Fig 1.3: Schematic of perovskite with center cation surrounded by eight BO_6 tetrahedra [4].

Perovskites can take different symmetries such as cubic, tetragonal, orthorhombic, and rhombohedral depending on the tilts and rotation of the TiO_6 octahedra. However, not all crystal structures will exhibit ferroelectricity, if there is no way to generate a net dipole moment. Cubic perovskites cannot show ferroelectricity because it has a center of symmetry, and no net dipole moment is generated. However tetragonal, orthorhombic, and rhombohedral crystal structures can

fulfill the requirements of lacking a center of symmetry. For example, in the tetragonal case, the *c*-axis is elongated, and the center positively charged ion moves up (or down) relative to the negatively charged oxygen, inducing a permanent dipole moment [5]. This example is shown in Fig 1.4.

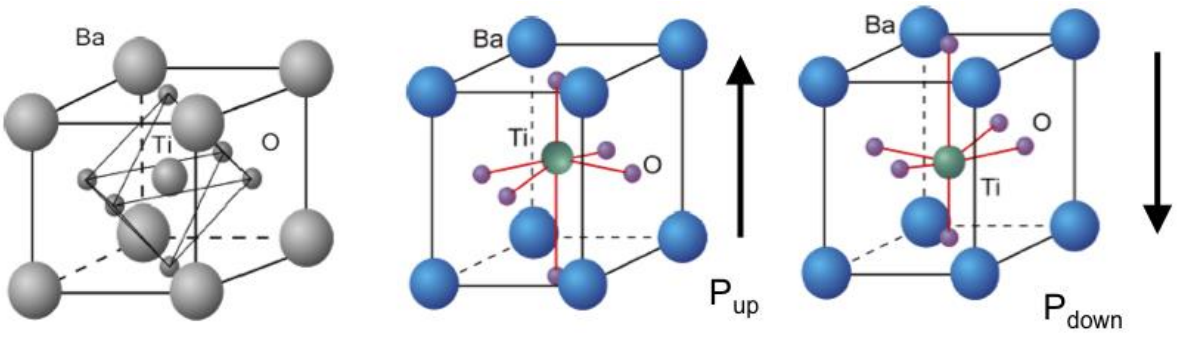

Figure 1.4: Ferroelectric materials must lack a center of symmetry to have a polarization. (a) $BaTiO_3$ with a cubic crystal structure and no polarization. (b,c) Tetragonal $BaTiO_3$ with polarization up and down

One of the key attributes of ferroelectric systems, in addition to spontaneous polarization, is having switchable polarization along a polar axis. The polar axis is identified as the direction of the polarization vector. For example, the tetragonal unit cell has its polar axis along the [001] *c*-axis as described in Fig. 1.5. In the case of orthorhombic and rhombohedral unit cells, the polar axes are along the [111] and the [110] directions respectively, as shown in Fig. 1.5.

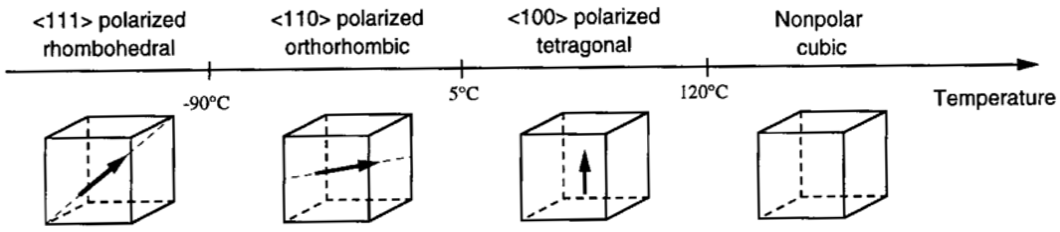

Fig 1.5: Evolution of $BaTiO_3$ structural phases and polarization directions with temperature [9].

1.3: Domains and domain walls

A domain is considered a region where the order parameter is aligned in the same direction, as displayed in Fig. 1.5. As a result of competition between elastic, electrostatic, and domain-wall energies – thin film ferroelectrics tend to break into nanodomains with certain directions of their polarization axes. Understanding behavior of domain walls can allow for development of novel nanoelectronic devices [6].

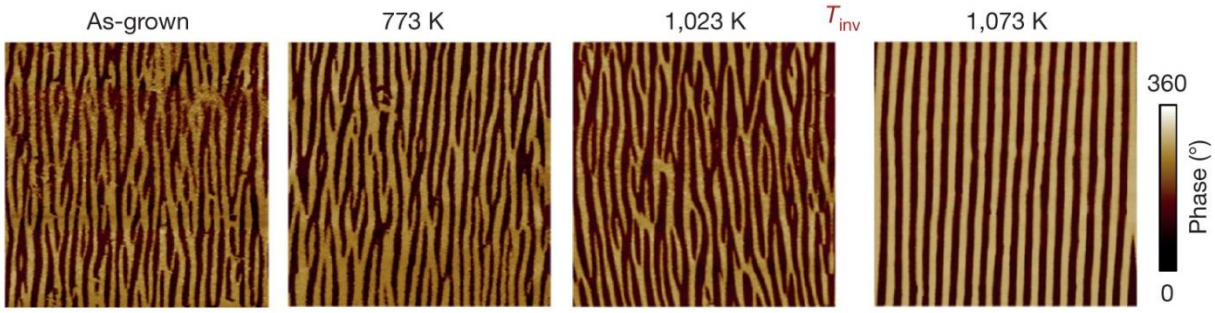

Figure 1.6: In-plane piezoresponse force microscopy (PFM) phase images of a 95-nm thick $BiFeO_3$ film grown on a (110) orthrohombic-oriented $DyScO_3$ substrate, for the as-grown sample, and the same sample after annealing at 773 K, 1,023 K and 1,073 K. The images are 5 × 5 μm^2 [7].

Ferroelectric domains tend to be categorized by the direction of the polarization vector in reference to the crystallographic axes. For example, domains that have polarization out-of-plane are typically referred to as *c*-domains, while domains with in-plane polarization vectors are referred to as *a*- or *b*- domains. A few examples of how these domains look is shown in Fig. 1.7 [8].

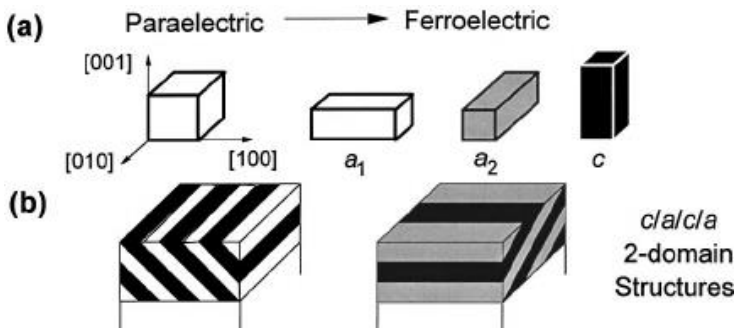

Figure 1.7: (a) Domains defined along crystallographic axes, (b) example schematic of c/a/c/a domains [9]

Boundaries between domains are classified as domain walls. Whether a domain will form is a balance between the energy gain of the system by breaking into domains, and the energy cost to form domain walls [5]. There are a few common types of ferroelectric domain walls, including 180° domain walls, 90° walls, charged head-to-head walls, insulating tail-to-tail walls, and neutral side-by-side walls, as shown in Fig. 1.8. Ferroelectrics like $BiFeO_3$ (BFO) can also form 71° and 109° domain walls due to the direction of the polar axis since BFO is rhombohedral [6]. Domain walls tend to have preferential ordering in certain crystallographic directions in order to minimize stresses. Some examples of how domains can order are shown in Fig. 1.9. In some ferroelectric materials, specific domain patterns are only stable in certain temperature ranges and can spontaneously transition across temperature [10].

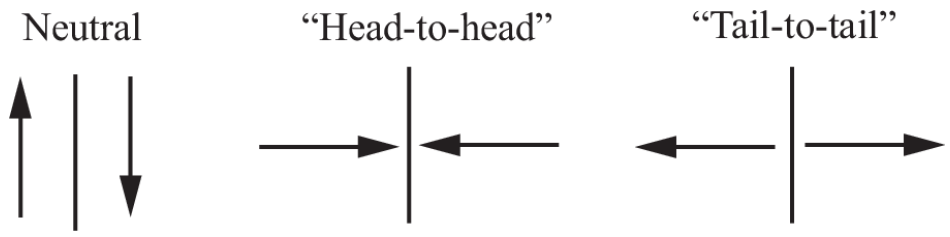

Figure 1.8: Example of neutral, "head to head", and "tail to tail" 180° domain walls [11].

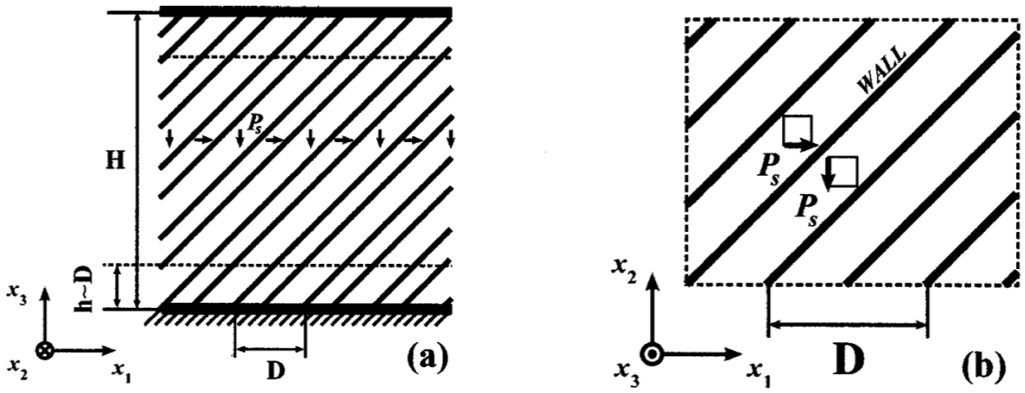

Figure 1.9: (a) Schematic of a/c/a/c domain ordering along the [101] direction, (b) schematic of a/b/a/b domain ordering the [110] direction. Here, P_s refers to the polarization vector in each domain and D refers to the domain periodicity [10].

1.4: Barium titanate ($BaTiO_3$)

The main material of interest for my thesis will be $BaTiO_3$, which is a model ferroelectric system with the perovskite crystal structure. $BaTiO_3$ consists of a Ti^{4+} atom in the center, Ba^{2+} in the eight corners and O^{2-} in the face centers as shown below in Fig. 1.10.

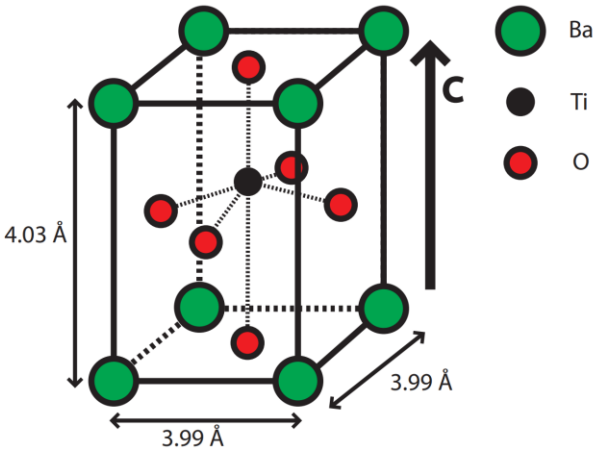

Fig 1.10: Example unit cell for $BaTiO_3$ with a tetragonal distortion along the c-axis. The center ion is shifted vertically up from the middle position, which gives the material a net dipole moment [5].

The Curie temperature (T_C) occurs at 120°C, where above this temperature, the material has cubic symmetry. Below T_C, the material transforms to a tetragonal structure where Ti ions are displaced vertically or horizontally away from the anions, causing a net polarization along the ⟨001⟩ directions. This means there are six possible polarization directions at this temperature. At 5°C, $BaTiO_3$ transforms from tetragonal to orthorhombic crystal structure where the cation displacement is along the ⟨110⟩ directions, leading to twelve possible polarization axes. Finally, at -90°C, $BaTiO_3$ undergoes a transition to a rhombohedral crystal structure where the cations displace along one of the cubic ⟨111⟩ directions, for which there are eight possible polarization axes. The phase diagram of $BaTiO_3$ is shown in Fig. 1.11 [12].

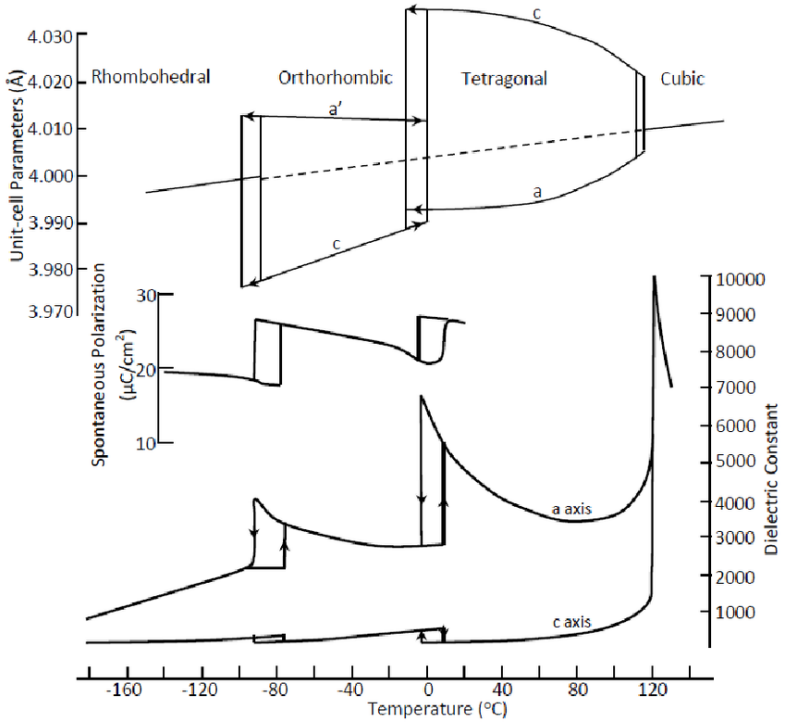

Figure 1.11: Lattice parameters and relative permittivity of $BaTiO_3$ as a function of temperature, showing four phases with distinct crystal symmetries [12].

As a thin film, $BaTiO_3$ tends to break into nanodomains of alternating polarization directions in order to minimize the free energy. The Landau-Ginzburg-Devonshire (LGD) model has been used to predict a rich phase diagram of ferroelectric domain ordering as a function of misfit strain and temperature as shown below in Fig. 1.12. Here, misfit strain is defined as,

$$S_m = (a_{film} - a_{substrate})/(a_{substrate})$$

Different phases present in Fig. 1.12 are defined by the direction of polarization axis in the domains. For example, the *a*/*c* configuration refers to domains of alternating polarization along the *a*- axis and along the *c*-axis. Note that in *a*/*b* domains along the in-plane crystallographic axes are referred to as a_1/a_2 in Fig. 1.12.

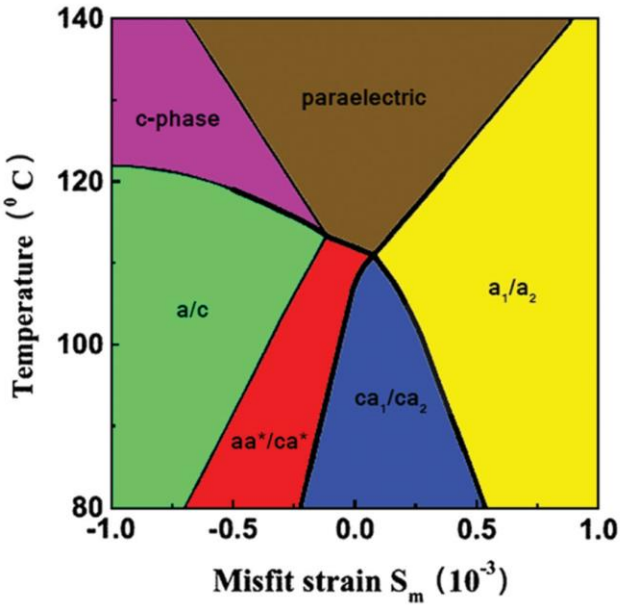

Figure 1.12: Phase diagram of ferroelectric domain ordering in $BaTiO_3$ as a function of temperature S_m, predicted by A. Everhardt et al. using the LGD model [13].

Tuning misfit strain in thin film $BaTiO_3$ by choice of the substrate allows for a wide range of possible ferroelectric domain systems. Recently A. Everhardt *et al.* have shown the feasibility of

growing $BaTiO_3$ on $NdScO_3$ to offer both *a*/*c* and *a*/*b* domains. Low strain $BaTiO_3$ undergoes a domain reorientation transition (T_R) near 50°C where domains transition from *a*/*b* to *a*/*c* domain polarization ordering. Additionally, the direction of domain walls also transforms from ordering along the (110) plane to the (010) plane above T_R. Piezoelectric force microscopy (PFM) has been used to image domain patterns at different temperatures to confirm domain polarization, periodicity, length, and preferential orientation as shown in Fig. 1.13. At 25°C, there are visible 90° in-plane domains with domain walls that order along the [110] direction, consistent with the domain pattern for *a/b* domains. At 70°C, domains are rotated by 90° where domain walls become parallel to the (010) plane. It can be deduced that this ordering comes from *a/c* domains, but Everhardt *et al*. performed further characterization to confirm the out-of-plane polarization [13].

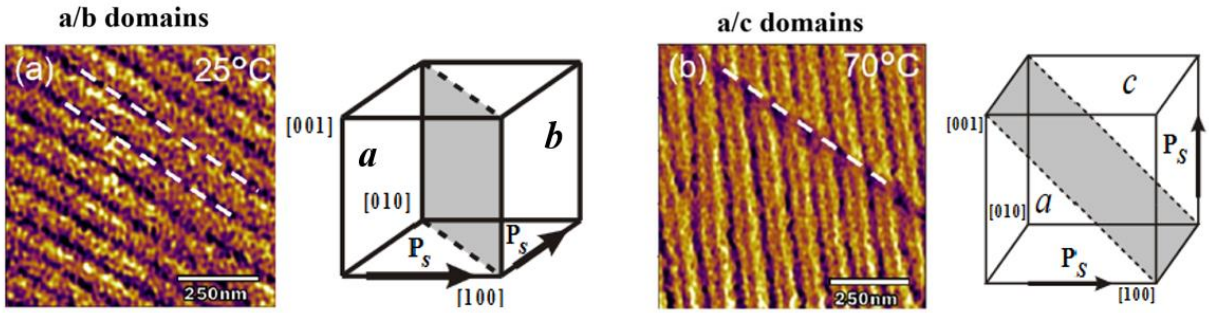

Figure 1.13: Lateral PFM image of (a) a/b domains and (b) a/c domains with respective schematic of each unit cell. Information about relative amplitudes from PFM images can be found in Everhardt et al. [10,14].

In-plane and out-of-plane XRD reciprocal space maps (RSM) were performed for varying peaks and temperatures as shown in Fig. 1.13. Evidence of domains show up as intensity modulation off of the Bragg peak, often reffered to as satellite peaks. Here, satellite peaks arise due to scattering from the periodic arrangement of ferroelectric domains and appear in specific *q*-spaces based on periodicity and ordering of domains. Below T_R, RSM's were taken at the (100), (110), and (001) Bragg peaks. All of these measurements showed evidence of satellite peaks from *a*/*b* domain

ordering along the [110] direction with a real space periodicity of 100 nm, consistent with PFM images. Above T_R, RSM's were taken at the (010), (100), and (001) Bragg peaks which similairly showed evidence of *a*/*c* domain ordering due to intensity modulations along the [010] direction with periodicity of 70 nm [13]. Some of the RSM's such as Fig. 1.14a and Fig. 1.14b also show higher orders of domain satellite peaks. Due to the larger periodicity of domains in real space, the ordering becomes closer together in reciprocal space and can be more accessible in a smaller *q*-space range. Higher order peaks come from the integer value *n* in Bragg's law, which will be discussed in the following chapter.

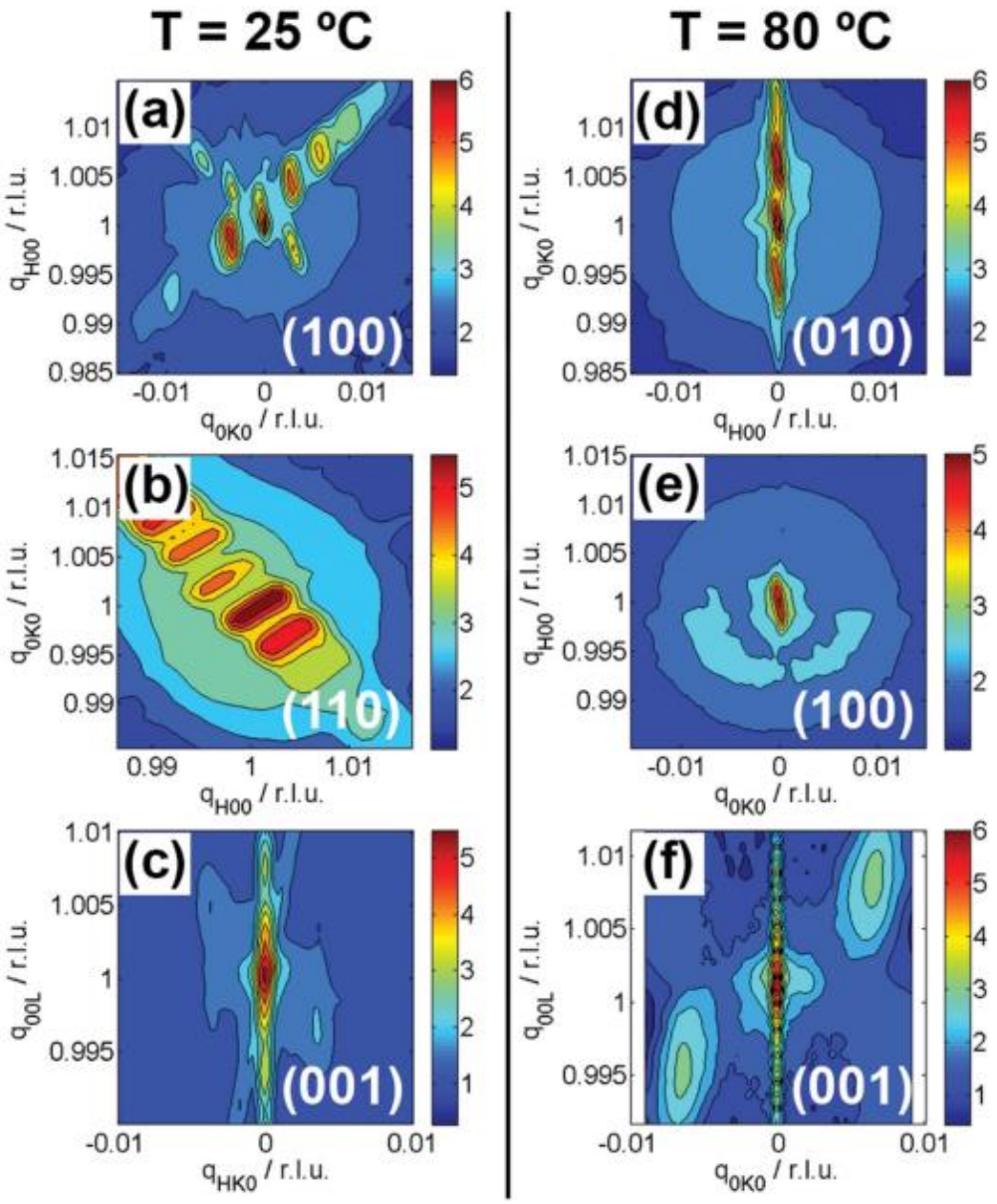

Figure 1.14: RSM around a) (100), b) (110), and c) (001) Bragg peaks at room temperature; RSM around d) (010), e) (100), and f) (001) Bragg peaks at 80 °C. Colors are in log(10) scale [13]

In addition to the symmetric RSM measurements, a few measurements were also taken for asymmetric peaks such as (204) in order to confirm epitaxial growth with existence of domain scattering, as shown in Fig. 1.15.

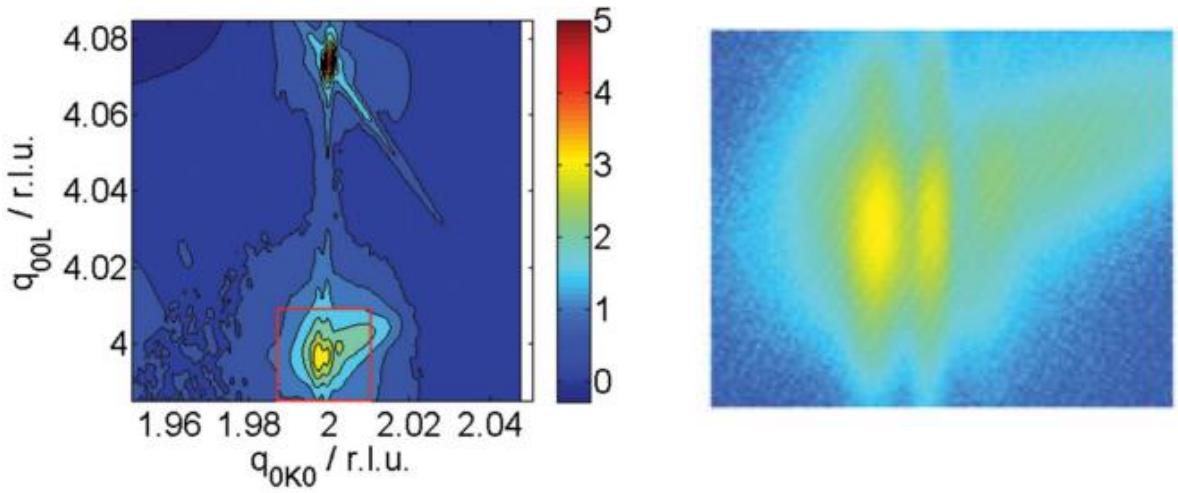

Figure 1.15: (Left) RSM of (204) peak showcasing $NdScO_3$ substrate at the top and the $BaTiO_3$ peak near the bottom with evidence of domain scattering to the side. (Right) Close-up of $BaTiO_3$ peak in the red square [13].

1.5: Fluctuations in ferroelectrics:

While ferroelectric domain ordering and reconfiguration have been experimentally observed and theories have been developed to predict these transitions, it is still unclear what are the driving mechanisms for domain transformations. Some systems indicate that domain reconfiguration can be driven by enough thermal energy to overcome reconfiguration barriers, in accordance with simple free energy arguments. However, disordered systems with degenerate energy states or multiple states that are close in energy can give rise to spontaneous fluctuations. Spontaneous fluctuations could then drive domain reconfiguration. Domain reconfiguration is closely linked to the overall switching behavior of ferroelectric materials and understanding domain fluctuations could play a role in optimizing domain patterns. Careful studies of fluctuations in ferroelectric domains can help understand and control domain stability and reconfiguration both near and far from various transitions.

Recently, ferroelectric domain fluctuations were measured for striped domains in a $PbTiO_3/SrTiO_3$ superlattice by Q. Zhang *et al*. It was shown that temperature increases (closer to the T_C), fluctuation timescales are faster. Using an Arrhenius temperature dependence, it was estimated that the effective activation energy of domain fluctuations was 0.35 ± 0.21 eV, as shown in Fig. 1.16. While there is likely a large uncertainty in the activation energy due to the lower goodness of the fit, it is still useful in understanding potential driving mechanisms for fluctuations. The estimated activation energy is lower than the activation energy for diffusion of oxygen vacancies, which is a known pinning site for domain walls, therefore it is speculated that formation and annihilation of structural defects could be driving the fluctuations [15].

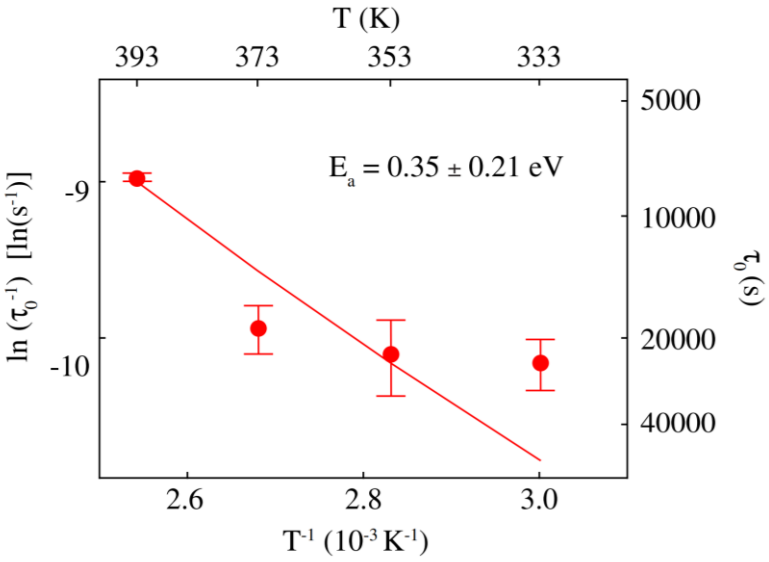

Fig 1.16: Decay constant fits for $PbTiO_3/SrTiO_3$ superlattice as a function of temperature with an Arrhenius fit to estimate activation energies of domain fluctuations [15].

Li *et al*. have also conducted fluctuation studies for *a*/*c* domains in $BaTiO_3$ as they reconfigure at the T_R and near T_C. Data scans were taken from a temperature range from 40°C to 125°C, where T_R (the *a*/*b* to *a*/*c* domain transformation) occurs near 50°C and the T_C is around 130°C. From the

experimentally obtained decay constants at different temperatures, it was shown that the *a*/*c* domains are particularly stable well below the transition, but then undergo higher fluctuations as T_R is approached, and then re-stabilize when temperature is greater than T_R. Near T_C, the fluctuations also vary as a function of temperature. Decay constants for each temperature are plotted in Fig. 1.17. The activation energy was also estimated and was found to be 0.67 ± 0.27 eV. This is also close to the activation energy of oxygen vacancy migration and the generation and annihilation of topological defects which is another reported mechanism for fluctuations of domain patterns [16].

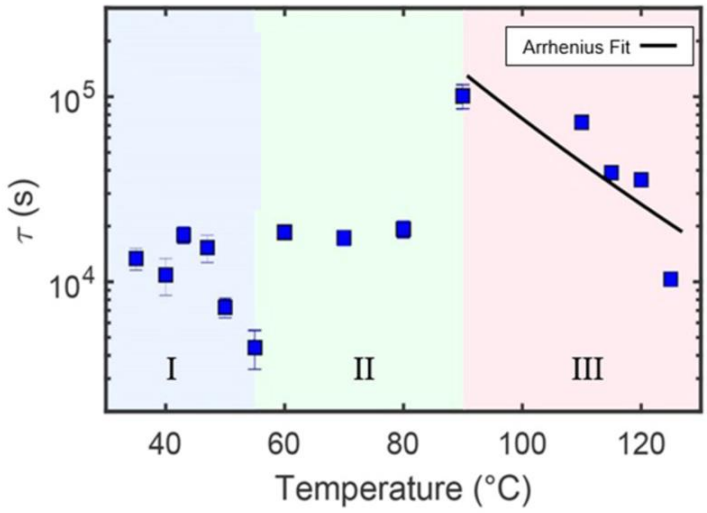

Figure 1.17: Decay constant fits for low strain $BaTiO_3$ thin film as a function of temperature with an Arrhenius fit to estimate activation energies of domain fluctuations [16].

The studies conducted by Li *et al.* present critical findings about thermal fluctuations in $BaTiO_3$ but are only for *a*/*c* domains. My thesis focuses on the dynamics of *a*/*b* domains in $BaTiO_3$ and compares it to *a*/*c* domain fluctuations.

1.6: Project objectives and open questions

In this thesis, I focus on investigating the fluctuation dynamics of the low temperature *a*/*b* domains across the domain reorientation transition (T_R) around 50°C in $BaTiO_3$. While the LGD theory discusses possible free energy terms to describe the behavior of ferroelectric domains, it neglects the contribution of domain fluctuations. Its main assumption is that fluctuations in the order parameter (polarization for ferroelectric materials) are significantly lower than the magnitude of the order parameter itself. Thus, fluctuations are only critical at transition temperatures [8]. However, the influence of domain fluctuations poses to be very crucial for both domain stability and domain switching. This research aims to answer several questions regarding dynamics of ferroelectric domains in $BaTiO_3$, with the main goal of understanding fluctuation dynamics of *a*/*b* domains in $BaTiO_3$.

1. How do fluctuations play a role in domain reorganization in $BaTiO_3$? Does the stability of *a*/*b* domains evolve as a function of temperature, particularly near the domain reorientation transition? How do these fluctuations compare to dynamic behavior in *a*/*c* domains?
2. How do higher order domain scattering peaks compare in their fluctuation behaviors?
3. Is there a *q*-dependence in fluctuation behavior within a peak?

My thesis addresses these questions by analyzing time dependent responses of scattering from *a*/*b* domains in a low strain $BaTiO_3$ film from room temperature to 65°C across the domain reorientation transition near $T_R \sim 50°C$. In these studies, we are able to access and compare several orders of diffraction peaks from domain scattering, as well as comparing between different *q*-ranges within a peak.

1.7: Summary

The goal of this chapter is to introduce ferroelectric materials and provide a motivation for investigating fluctuation dynamics of ferroelectric domains in $BaTiO_3$. This study aims to fill research gaps regarding the reorientation transition from *a*/*b* to *a*/*c* domains in $BaTiO_3$ and exploring possible *q*-dependence of domain scattering. In Chapter 2, relevant experimental techniques will be discussed such as thin film synthesis, x-ray scattering, and x-ray photon correlation spectroscopy (XPCS). In Chapter 3, I will discuss my results and discussion about time dependent characteristics of *a*/*b* domain fluctuations. In Chapter 4, I will summarize my outcomes and conclude with some thoughts on future prospects.

Chapter 2: Experimental methods

In this chapter, relevant background to experimental methods and techniques is provided. First, I discuss details of the sample used and thin film synthesis techniques. The low strain $BaTiO_3$ sample was fabricated using pulsed laser deposition by Dr. A. S. Everhardt and Dr. S. Matzen in Dr. B. Noheda's group at the University of Groningen using pulsed laser deposition. Fluctuation dynamics of the ferroelectric domains were investigated using x-ray photon correlation spectroscopy (XPCS) at the Coherent Hard X-Ray (CHX) beamline at the National Synchrotron Light Source (NSLS-II) in Brookhaven National Laboratory (BNL). The chapter will describe pulsed laser deposition, x-ray scattering, synchrotron sources, and x-ray photon correlation spectroscopy (XPCS).

2.1: Sample fabrication

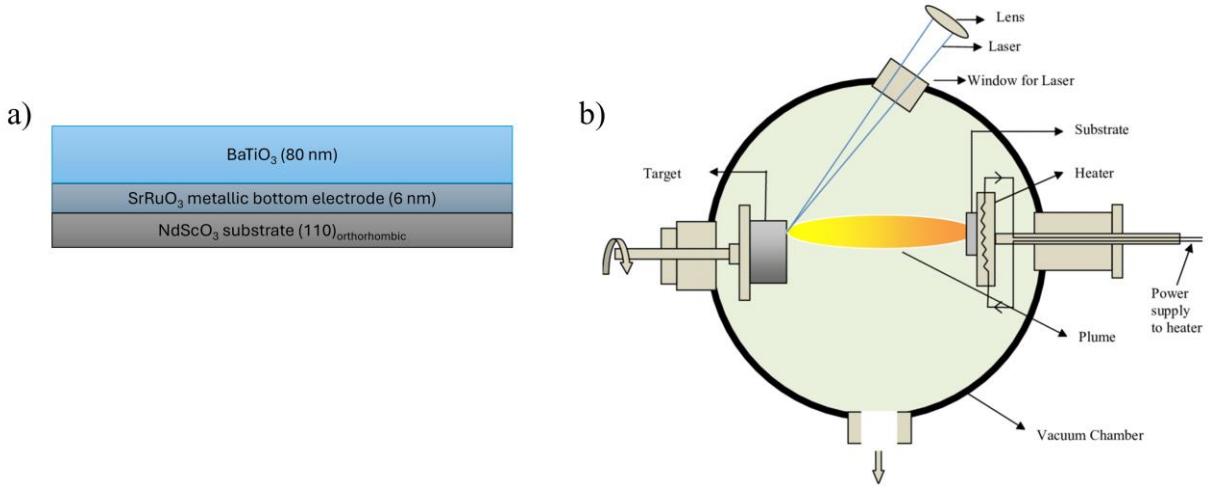

Figure 2.1: (a) Schematic of $BaTiO_3$ sample. (b) Components in a pulsed laser deposition chamber.

The film used in this research was fabricated by our collaborators Dr. A. S. Everhardt and Dr. S. Matzen in Dr. B. Noheda's group using pulsed laser deposition (PLD). The sample is an 80 nm

thin film of $BaTiO_3$ grown on a $NdScO_3$ $(110)_{ortho}$ substrate with a fully strained 6 nm bottom electrode of metallic $SrRuO_3$. The substrate and bottom electrode were chosen to optimize a misfit strain (nominally -0.05%) on the sample that would enable an *a*/*b* and *a*/*c* domain configuration. Schematic of the sample stack is shown in Fig. 2.1.

PLD is a thin film synthesis technique which is part of a larger category of thin film processing known as physical vapor deposition. PLD is an ablative process where the surface of the target material is physically ablated by a laser and target atoms are ejected into the deposition chamber. The ejected atoms create a plasma plume of ionized atoms which are directed towards the substrate and can adhere on the surface of the substrate to create layers of material, as shown in Fig 2.1. Some advantages of PLD are having precise control of thickness, composition, and high epitaxial quality.

For the $BaTiO_3$ sample used in this thesis, a Lambda Physik COMPex 25 Pro 205 KrF (λ = 248 nm) excimer ultraviolet laser was used for the PLD growth with the following growth parameters: background pressure of 10^{-7} mbar, a substrate temperature of 700–800°C, a laser energy of 2 J/cm^2, a spot size of 2.6 mm^2, a target-substrate distance of 50 mm, a repetition rate of 5 Hz, cooling rate of 5°C per minute at 300 mbar partial pressures of O_2 after the growth and the growth partial pressures O_2 was varied between 0.15 and 0.20 mbar.

2.2: X-ray scattering

X-rays are electromagnetic waves with wavelengths on the order of an angstrom (10^{-10} m) to nanometers (10^{-9} m). The interaction of light with matter leads to two general outcomes: scattering or absorption. In the case of scattering, the classical description of x-rays depicts a scattering event as the wiggling of total atomic electron clouds followed by a re-emission of the incident x-ray into

random orientations. Specifically, *elastic scattering* occurs when the incident and scattered x-rays have the same wavelength, i.e. $|k| = |k'|$ where *k* is the incident wavevector and *k'* is the scattered wavevector. Elastic x-ray scattering is the basis of many techniques used to encode structural information of materials, originally discovered as *Thomson scattering* [17].

To understand scattering from a material, it is often easier to start with one electron and build up to a lattice. The ability of an electron to scatter is considered the *scattering length* ($f(\epsilon, \epsilon')$), includes information such as the scattered amplitude and polarization:

$$f(\epsilon, \epsilon') = -\frac{re^{-ik'r}}{E} E' \cdot \epsilon'$$

Here, $e^{-ik'r}$ is the spherical wave form of the x-ray, *E* is the incident light, *E'* is the scattered light, and ϵ' is the polarization direction [17]. The *differential scattering cross section* is defined from the scattering length below as,

$$\frac{d\sigma}{d\Omega} = |f(\epsilon, \epsilon')|^2$$

Differential scattering cross section is also defined as a ratio of photons recorded on a detector over the flux of the incident beam with a solid angle correction. This is given by,

$$\frac{d\sigma}{d\Omega} = \frac{I_{sc}}{\Phi_0 \Delta\Omega}$$

where I_{sc} is the number of scattered photons per second recorded by the detector, Φ_0 is flux of the incident beam, and $\Delta\Omega$ is the solid angle which the x-ray subtends [18].

The scattering cross section can be thought of as the efficiency of scattering in a particular direction for a specific scatterer, as shown in Fig. 2.2. The total cross section can be found by integrating the differential cross section over all possible scattering angles (2π) [18].

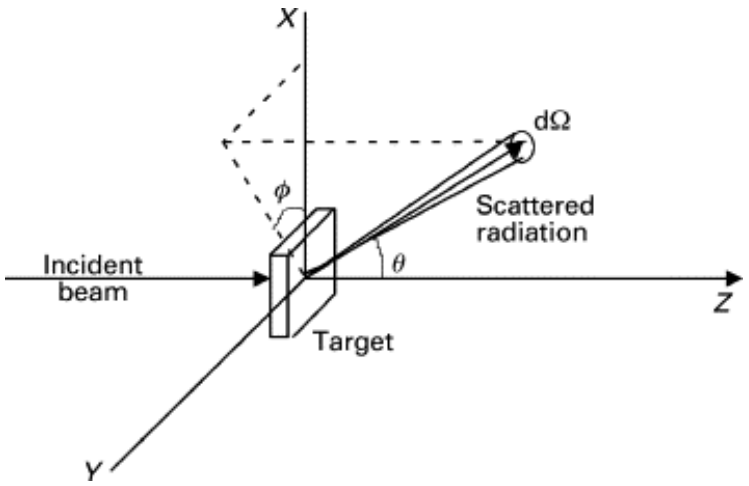

Figure 2.2: Schematic of scattering cross section with incident beam, sample, and scattered radiation [19].

Scattering from an atom is considered as the next step, as shown in Fig. 2.3. Here, the important distinction in the scattering length and cross section is the introduction of the *atomic form factor* $f(Q)$ which is a positive number that relates the number of electrons in an atom. The equation for $f(Q)$ is defined as follows,

$$f(Q) = -\frac{1}{e}\int \rho(\boldsymbol{r})\, e^{iQr}\, d\boldsymbol{r}$$

where $f(Q)$ is the atomic form factor, and $\rho(\boldsymbol{r})$ is the spatial density of the scatterer. The atomic form factor considers the response of all Z electrons, disregarding inter-shell resonant electronic transitions. Quantitatively, it is the Fourier transform of the spatial density $\rho(\boldsymbol{r})$ multiplied by $-1/e$.

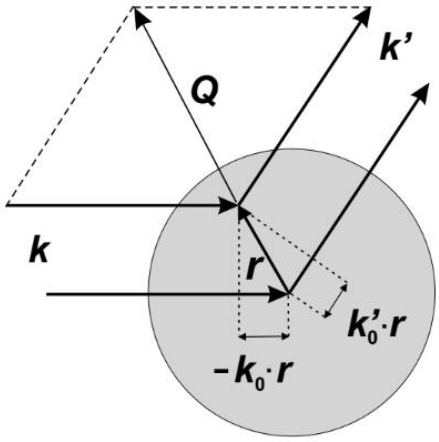

Figure 2.3: Schematic of scattering from an atom where the incident wave vector, ***k****, is scattered as* ***k'****. The momentum transfer between the two is shown as* ***Q*** *=* ***k-k'****. [17]*

It is now possible to define scattering in terms of a periodic lattice in a crystal. This is done by deriving a *structure factor* (F_{hkl}) for the unit cell, which relates amplitude of diffraction signal for a distribution of atoms in a unit cell [17]. This is defined as,

$$F_{hkl} = \sum_{j=1}^{N} f_j(q)\, e^{iq \cdot \boldsymbol{r}_j}$$

where $f_j(q)$ is the atomic scattering factor for the jth atom and r_j is the location of the atom in the unit cell. In the equation above, the atomic form factor, *f*, is tabulated for elements when using the proper scattering angle and *hkl* reflection. The structure factor, F_{hkl}, is also related to diffracted intensity in the following way,

$$I_{hkl} \propto |F_{hkl}|^2$$

Solving the structure factor for a specific unit cell can be used to calculate which *hkl* peaks will diffract and the intensities of each peak. To better understand diffraction, the simplest example is *Young's double slit experiment*, which is shown visually in Fig. 2.4. This experiment begins with

a light source, such as a laser, that shines through a material with two parallel slits. The original experiment used a lamp and a pinhole to create coherent light. When the light passes through the two slits, the beam acquires different path lengths and therefore phase differences. The resultant wavefronts then undergo constructive and destructive interference which results in alternating bright and dark bands on a screen that decay sinusoidally in intensity. This is the basis of diffraction, where light can interact with a grating and result in a pattern of intensity representative of the diffraction grating. For the double slit diffraction experiment, the diffraction grating only consists of two slits. However, this can be expanded to an experiment with any number of slits, as the only requirement for a diffraction grating is to have a repeating pattern. Applying this concept to x-ray diffraction of crystalline materials, we can think of lattice planes as a diffraction grating for x-rays and the constructive and destructive interference of diffracted wavefronts will appear as a diffraction pattern where high intensity regions are labelled as Bragg peaks [17].

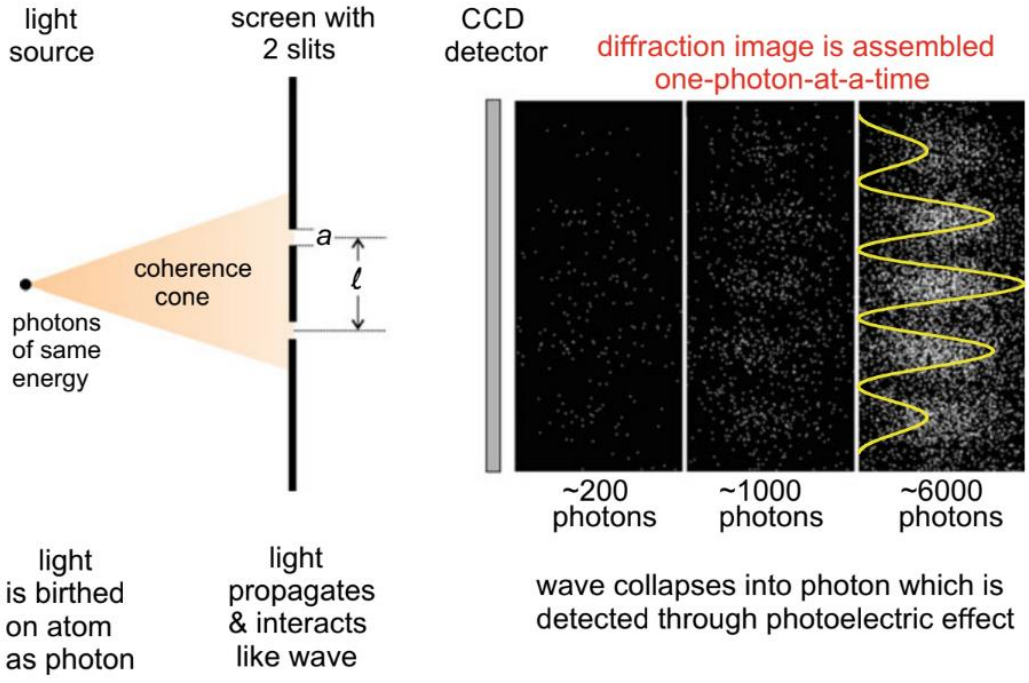

Fig 2.4: Schematic of double slit diffraction experiment [17].

Thomson scattering from a crystalline material has been commonly referred to as Bragg diffraction, or simply x-ray diffraction. This is based on the very simple equation from *Bragg's law*, which describes how a superposition of waves will constructively interfere from crystal lattice planes in a material. Bragg's law is derived as given by,

$$n\lambda = 2d \sin\theta$$

where n is the order of diffraction (typically kept at 1), λ is the wavelength of incoming x-ray, d is the spacing between lattice planes of interest, and θ is the angle of incidence. The geometry of Bragg's law derivation is in Fig. 2.5. This equation is useful in understanding diffraction experiments and calculating incidence angles for crystallographic peaks or planes of interest.

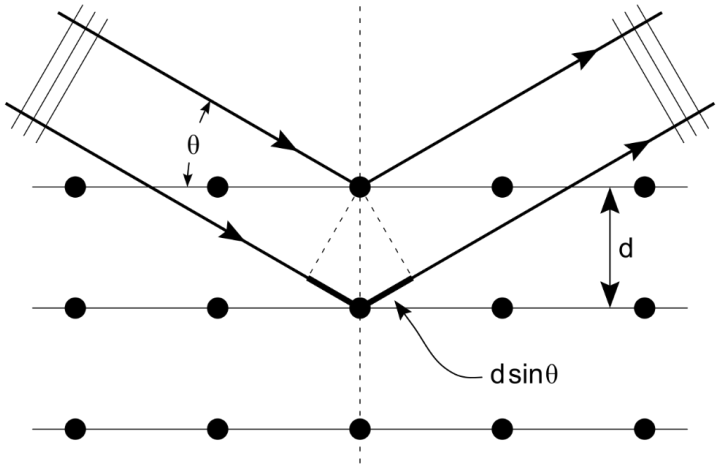

Figure 2.5: Example schematic of Bragg's law where two identical beams diffract off parallel planes in a crystalline solid. The lower beam must travel an extra path length of $2d \sin\theta$*, therefore constructive interference will occur at integer multiples of this value [20].*

Bragg diffraction can be used in different scan modes to characterize properties of thin films. For the purposes of this thesis, $2\theta - \theta$ scans and reciprocal space maps (RSM) were used. In a $2\theta - \theta$ scan, the sample motor and detector motor are moved in steps where if the sample moves by θ,

the detector moves by 2θ. This kind of scan gives information about lattice constants, strain and possible texture in the sample. Additional sample tilts are often required in thin film measurements due to offsets between the angle of diffracting planes and the sample surface. Therefore, the angle of the sample can also be referred to as ω, which arises from $\omega = \theta + \text{tilt}$. Fig. 2.6 shows geometrically where angles are in reference to a sample.

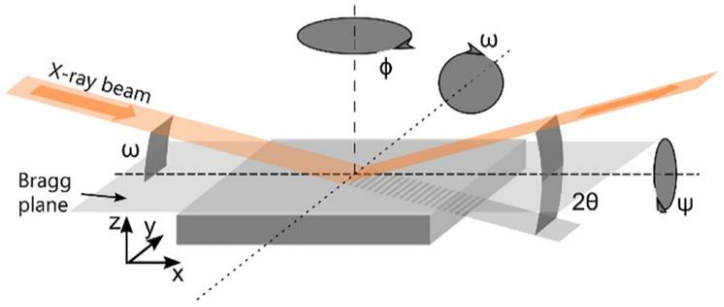

Fig 2.6: Example schematic of x-ray scattering with relevant angles in the geometry [21].

Reciprocal space maps are a way to visualize two dimensions of reciprocal space and access in-plane Bragg peaks. This is done by taking several $2\theta - \theta$ scans at slightly varying ω angles and plotting the intensities as a two-dimensional grid. With the use of 2D RSM's can be obtained at one angle without varying angles by individual steps, as shown in Fig. 2.7.

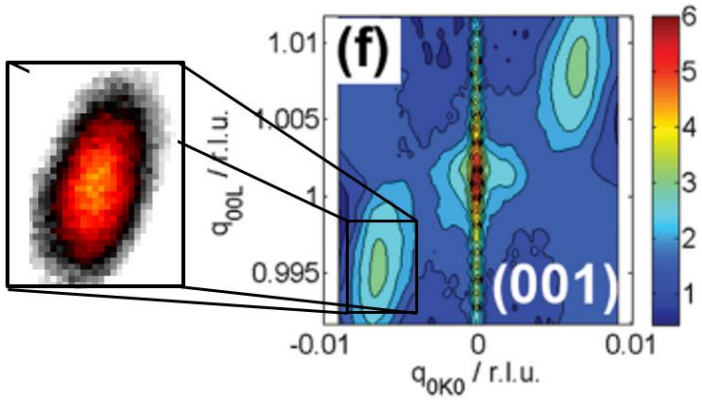

Figure 2.7: Example RSM with inset of x-ray scattering at the same peak using a 2D detector [13].

2.3: Synchrotron sources

While characterization methods using an in-house diffractometer can be useful in structural analysis of materials, there are some limitations in their capabilities. Synchrotron facilities offer high brilliance of x-rays, high coherence, ability to tune x-ray energy, and accessibility to faster timescales. My thesis utilizes synchrotron techniques due to their high coherence and high flux to encode local heterogeneities of domain fluctuations.

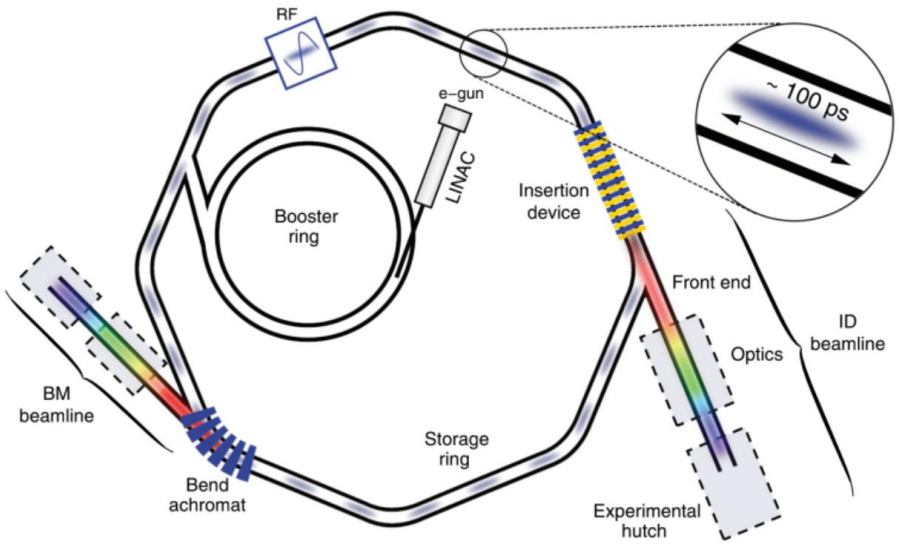

Figure 2.8: Schematic of a synchrotron source with relevant components as described in text [22].

The main components of a synchrotron include a linear accelerator (LINAC), booster ring, storage ring, insertion devices, and bending magnets, as shown in Fig. 2.8. Electrons are emitted from the LINAC by an electron gun as bunches and then gradually accelerated close to the speed of light. Before the electrons enter the storage ring, they are sent through a booster ring which continues to accelerate the electrons and increase energy of the electrons. Electrons can traverse the booster ring thousands of times before they are sent into the storage ring. Next, the storage ring is a type of particle accelerator which keeps electrons in a continuous particle beam. The storage ring will

have insertion devices and bending magnets along the path, as shown in Fig. 2.9. Most modern synchrotrons use undulators, which are periodic magnet structures which force the particle beam to "wiggle" or go through oscillatory motion. Bending magnets are kept at turns in the storage ring which help force the circular path of the beam in the storage ring. Derived from Maxwell's equations about the generation of electromagnetic fields from a charged moving particle, synchrotron radiation refers to the radiation of charged particles in a curved path. Both bending magnets and insertion devices are useful in ensuring synchrotron radiation is emitted and help produce monochromatic light [22].

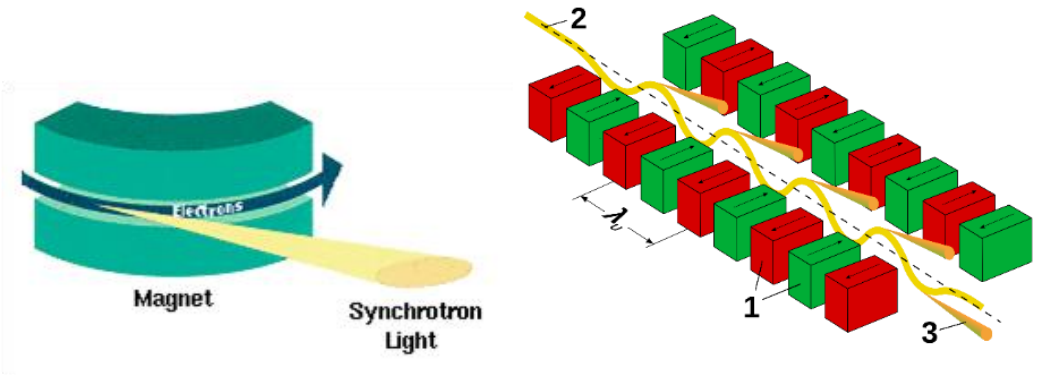

Figure 2.9: Schematic of synchrotron radiation from a bending magnet and a series of bending magnets, referred to as an undulator [23].

One of the primary advantages of synchrotrons comes from the fact that x-rays are highly collimated [18]. This gives many benefits such as high photon flux and brilliance. Third generation synchrotrons have been brighter than typical diffractometers by an order of 10^{12} in brilliance [18]. Brilliance can be defined by the flux as:

$$\text{Brilliance} = \frac{\text{Photons/second}}{(\text{mrad})^2(\text{mm}^2\ \text{source area})(0.1\%\ \text{BW})}$$

Additionally, outgoing x-rays have very high coherence. Coherence is critical for measuring fluctuations as scattering as it provides specific information about scatterers, rather than an average diffraction pattern as obtained from typical diffractometers. These kinds of diffraction patterns are typically referred to as "speckle" patterns, as shown in Fig. 2.10. More information about achieving coherence and speckles will be discussed in the following section [18].

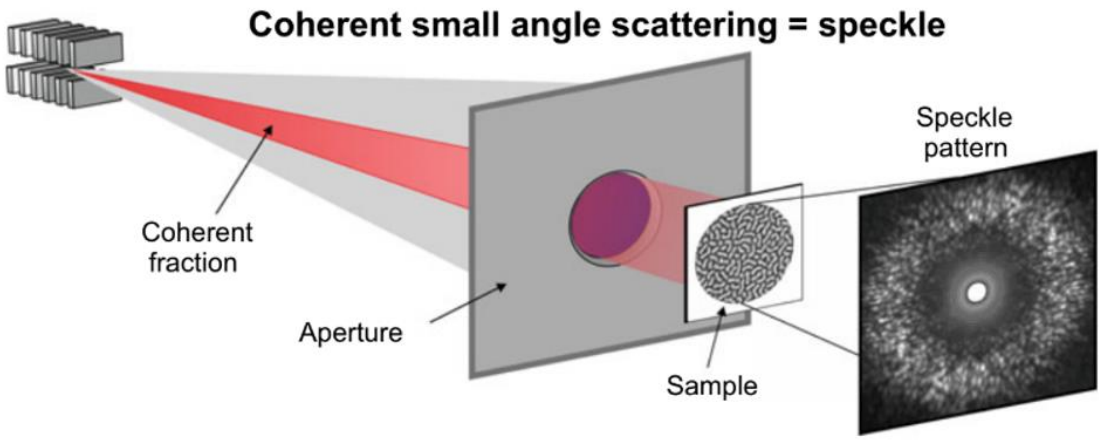

Fig 2.10: Example schematic of coherent scattering to generate speckle pattern by adjusting distance between the beam and sample as well as using a pinhole [17].

2.4: X-ray photon correlation spectroscopy

X-ray photon correlation spectroscopy (XPCS) is a powerful technique used to elucidate equilibrium fluctuations in materials. Results from XPCS experiments can be used to quantify characteristic time and length scales of atomic behavior in material systems. XPCS is the x-ray analog of dynamic light scattering (DLS), a technique used to quantify size distributions of molecules by correlating temporal fluctuations in scattered light. Since DLS typically operates in the visible regime of light (300-700 nm), it is commonly used to characterize particles and

polymers in suspensions or materials in the nanometer to micron length scale. With the advent of coherent x-rays in synchrotron sources, XPCS can be performed to characterize similar fluctuations of materials at the nanoscale. XPCS takes advantage of the highly coherent beam available at synchrotrons to produce detailed and accurate information about inhomogeneities such as domains, domain walls, defects, etc. This type of x-ray scattering resulting from a coherent light source is typically referred to as a *speckle* pattern, as shown in Fig. 2.11 [24].

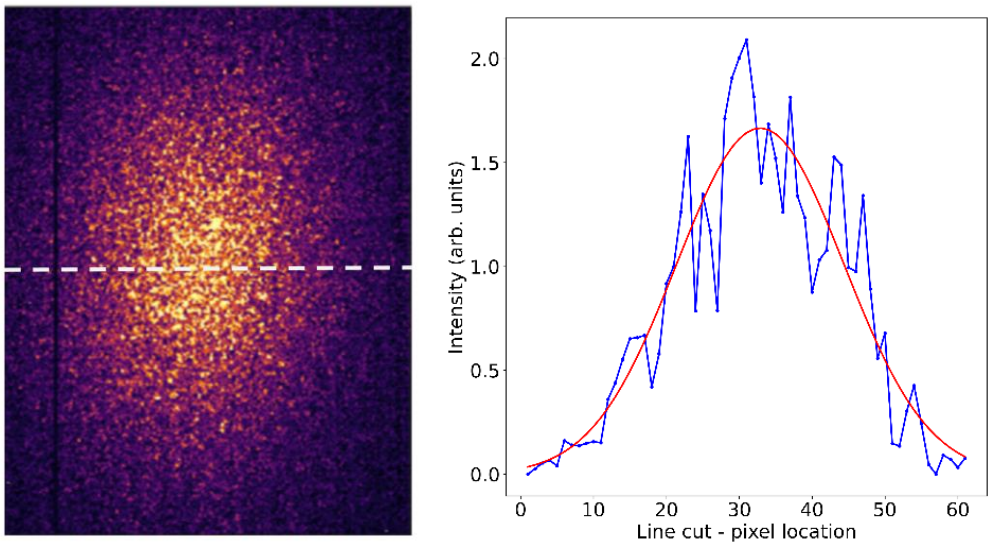

Figure 2.11: (Left) Speckle pattern with bright and dark intensity modulations. (Right) Line cut across speckle pattern with raw data in blue and a gaussian fit in red which represents scattering from incoherent beam [25].

2.4.1: Coherence

As mentioned previously, highly coherent beam is required to form speckle patterns for XPCS. Coherence is defined for both transverse (spatial) and longitudinal (temporal) directions of photon wave packets. Spatial coherence measures the correlation of a wave's phase on all points in space transverse to the direction of wave propagation. Spatial coherence can be determined by several things, including x-ray source size in the *y*- and *z*- directions (S_y and S_z assuming *x* is the direction

of x-ray propagation), angle of x-ray divergence ($\Delta\theta_y$ and $\Delta\theta_z$), and x-ray wavelength. The relationship between lateral coherence length (L_T), source size, and angular divergence is,

$$L_T = \frac{\lambda^2}{(S_y \Delta\theta_y S_z \Delta\theta_z)}$$

Temporal coherence measures the correlation of a wave's phase along points in time, or in the direction of wave propagation. This will be dictated by the monochromatic nature of the x-ray beam. This relationship is given by,

$$L_C \sim \frac{\lambda^2}{2\Delta\lambda}$$

where L_C is temporal coherence length, $\Delta\lambda$ is the range of wavelengths emitted and λ is the center of the range of wavelengths. Achieving enough spatial and temporal coherence for XPCS experiments is an ongoing challenge. Many synchrotron beamlines use a combination of different methods to improve coherence such as advanced focusing of the beam, changing the distance between the sample and source, and using a pinhole before the sample. A visual representation of spatial and temporal coherence is shown in Fig. 2.12.

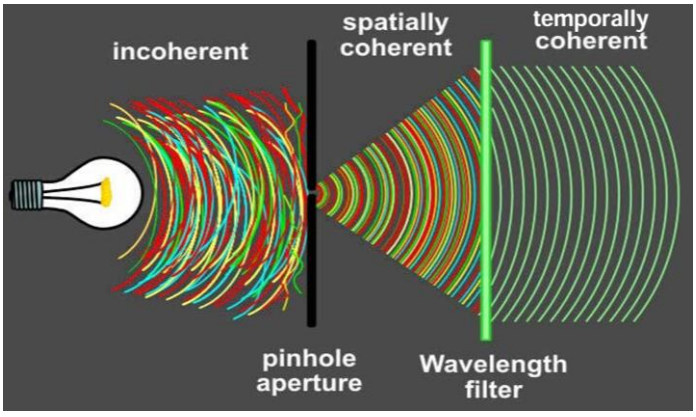

Figure 2.12: Spatial coherence occurs as uniform wavefronts in space while temporal coherence occurs as uniform wavelengths in time. The different colors represent a spread of wavelengths [26].

2.4.2: Experimental setup for XPCS

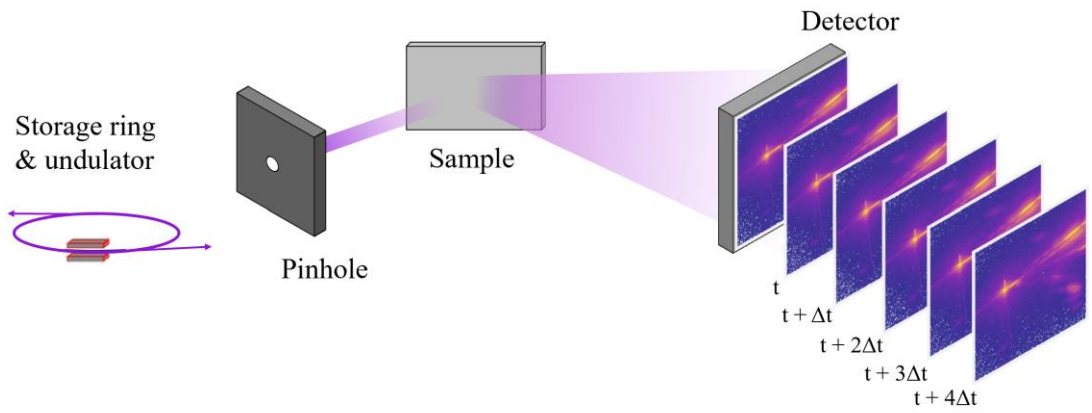

Figure 2.13: Schematic of an XPCS experimental setup. Spatially and temporally coherent x-ray beam from synchrotron is used to obtain speckle pattern as a function of time.

XPCS takes consecutive images of a speckle pattern over a desired scan time and correlate changes in intensity between each image of the scan, as shown in Fig. 2.13. The first step is to align any necessary optics to help improve coherency in the x-ray beam. Spatial coherence can be improved through using a pinhole which helps collimate the beam. However, using a pinhole decreases the intensity on the detector which can reduce signal-to-noise ratio (SNR). After ensuring that the optics are aligned as desired, the next step is to align the required scattering geometry for the sample. Depending on the material system and sample stack, transmission or reflection geometry can be used. Ultimately, each image will be correlated with each other to quantify miniscule changes in speckle intensity relating to changes in order and disorder in the system.

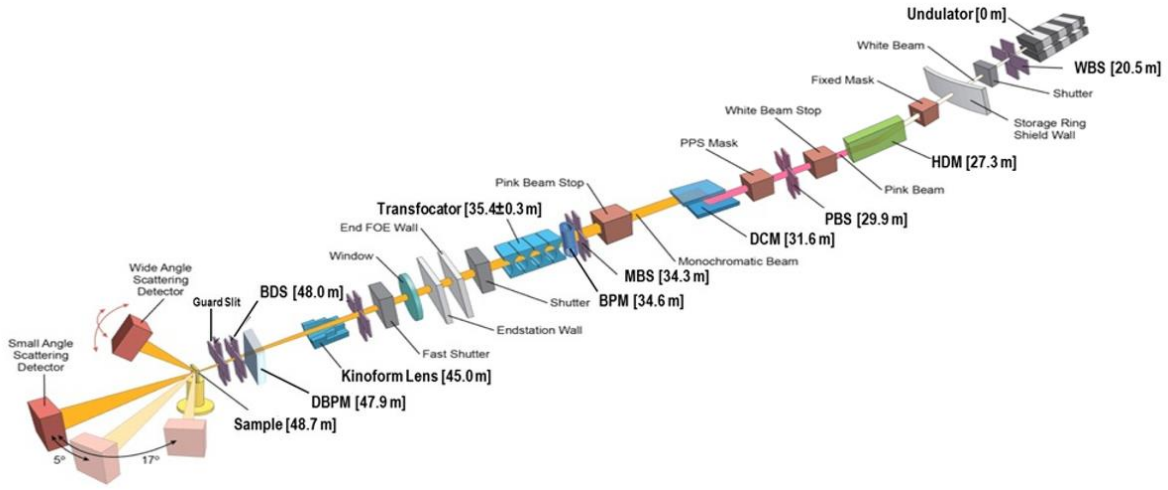

Figure 2.14: Schematic of CHX beamline at NSLS-II [27].

For this research, a series of XPCS scans were measured in the Coherent Hard X-ray Scattering (CHX 11-ID) beamline at the National Synchrotron Light Source II (NSLS-II) in Brookhaven National Laboratory (BNL). The coherent x-ray beam was at an energy of 12.8 keV and focused to a spot size on the $BaTiO_3$ sample of 3 μm on the sample. The scattered beam was collected onto a two-dimensional Eiger X 1M detector with a pixel size of 75 μm × 75 μm, positioned 1.5 m away from the sample. A detailed depiction of this beamline is shown in Fig. 2.14.

These scans were taken over a range of temperatures from 35°C to 65°C in step sizes of 5°C, ensuring to cover the T_R around 55°C. Each scan was three hours long where one image was taken every second, for a total of 10800 images per scan. In order to complement previously measured data of *a*/*c* domains in $BaTiO_3$, these measurements were taken at the (103) peak in order to access the in-plane *a*/*b* domains. The experiment was conducted in reflection geometry and the required angles were derived as 40.8749° in sample θ for the sample and 44.8871° in 2θ for the detector. However, the maximum angle in sample θ was limited to 21° at the beamline, therefore the sample was mounted on a 25° wedge to compensate for the extra tilt required, which is shown in Fig. 2.15.

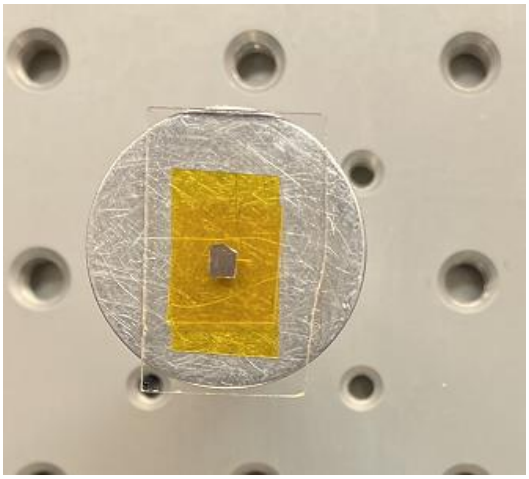

Fig 2.15: $BaTiO_3$ sample mounted on 25° wedge.

2.4.3: One-time correlation

In order to quantify the dynamics of associated fluctuations, correlation analysis can be used to relate changes in pixel intensity over time. Correlation is a mathematical technique which determines the similarity of observations at different instances. Some examples of this include temporal correlation or spatial correlation where correlation is done in either time or space. Autocorrelation is a specific correlation technique which determines the similarity of an observation with itself. This is done by increasing a delay between the observation and the "copy" of the observation and correlating the two instances [24]. Autocorrelation is one of the main mathematical tools used in XPCS analysis where intensity from a diffraction pattern taken at one time is correlated with another time as a function of time delay.

The one-time correlation function (g_2) is obtained by correlating the intensity of one pixel in time t to the intensity of the same pixel at time $t + \Delta t$ normalized by the average intensity of all the pixels, given by,

$$g_2(q,\Delta t) = \frac{\langle I_{ij}(q,t) I_{ij}(q,t+\Delta t)\rangle}{\langle I_{ij}(q,t)\rangle^2}$$

where q is the scattering vector, I_{ij} is the intensity of pixel with *i,j* position on the image, t is the real time that the frame was acquired, Δt is the time difference between frames, and brackets are used to indicate an ensemble average through all pixels. An example g_2 curve is given in Fig. 2.16.

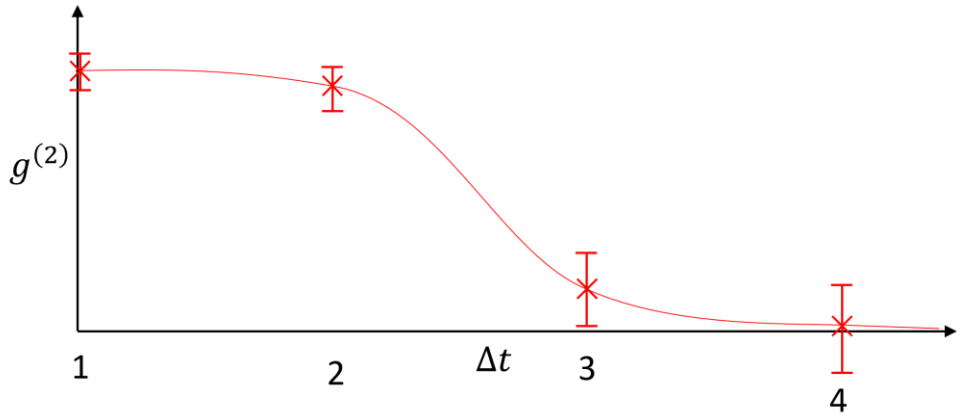

Figure 2.16: Example g_2 curve where the x-axis is time lag.

In Fig. 2.16, there are several key components to the curve g_2 curve shown above. First, it is important to note that the *x*-axis for g_2 plots is Δt refers to *time lag*. Since g_2 is calculated with respect to time lag, this means that the *x*-axis does not refer to real time but is referring to increasing the time between the frames that are being correlated. At $\Delta t = 1s$, the correlation will be the highest as this is a combination of each frame correlated with the very next frame, leading to small change between images. If $\Delta t = 2s$, this means that one frame is being correlated with another frame collected two seconds after. Increasing Δt will continue to increase the amount of time between frames which are correlated until the last point on the plot refers to correlation between the very first and the very last frame. This point will typically display the most amount of decorrelation that has occurred within the system for the specific XPCS scan, if the sample evolves

with time. Also, this will have extremely low signal to noise ratio (SNR) as only one set of data is available to calculate with.

One-time correlation is related to the intermediate scattering function (ISF) as,

$$g_2(q, \Delta t) = 1 + A|F(q,t)|^2$$

where A is the *Siegert factor* which defines speckle visibility through contrast, and $F(q,t)$ is the ISF. The *Siegert factor*, also often referred to simply as *contrast*, relays the intensity variation between the highest and lowest pixel intensity within the speckles being analyzed. The ISF can be fit using the exponential function,

$$|F(q,t)| = \left|\exp\left(-\frac{t}{\tau}\right)^{\beta}\right|$$

where τ is the decay constant and β is the fitting exponent. The decay constant is a parameter of how fast the ISF decays from full correlation to complete decorrelation, or how long the material system stays in stable. Shorter decay constants indicate faster fluctuations while longer decay constants indicate slower fluctuations and less dynamics. Additionally, β is a parameter that defines the shape or stretch of the exponential curve. This value is usually between 0 and 2 for similar systems. Typically, β larger than 1 indicates "jammed dynamics" where the system undergoes a sharp or sudden decorrelation. This is seen visually in Fig. 2.17 where the curve at 503K shows a gradual decrease in correlation while the curve for 443K starts off flat and then has a sharp drop at around $\Delta t = 10$ s. The fitting exponents are 0.72 and 1.42 respectively are indicated in Fig. 2.17. Additionally, $\beta = 1$ and $\beta < 1$ indicate diffusive and subdiffusive relaxation that is often found in glass-forming liquids and colloidal suspensions, respectively [28].

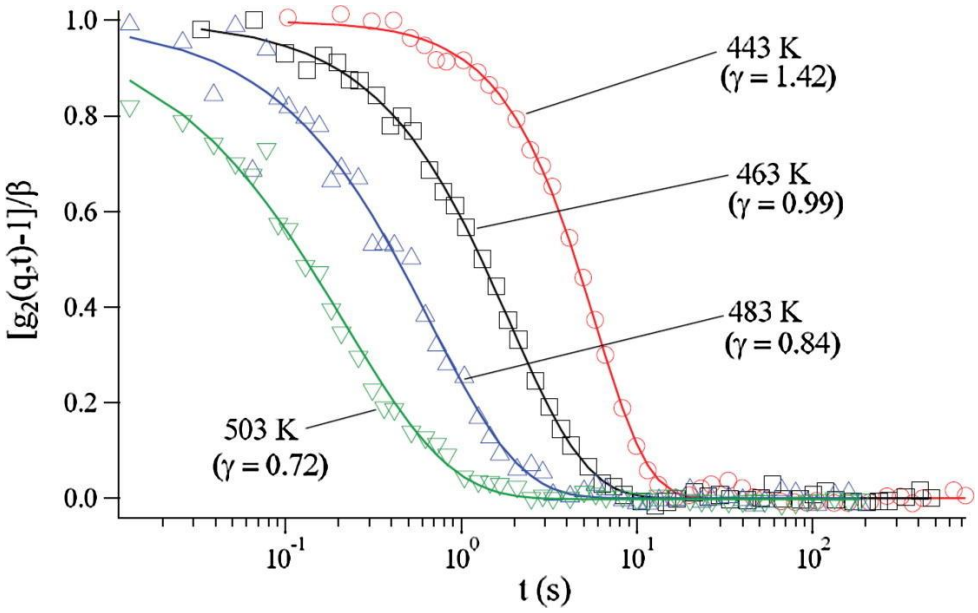

Figure 2.17: Normalized autocorrelation for nanoparticles dispersed in a matrix at different temperatures, solid lines are fits. [28]

2.4.4: Two-time correlation

While the one-time correlation function is a useful analysis to understand fluctuation dynamics of the XPCS scan, it is technically an average of all equivalent frames for Δt, i.e. time lag. Assuming the system is in equilibrium, averaging across all Δt frames is fine as the amount of fluctuation between frames is expected to be similar. However, if there are any non-equilibrium dynamics occurring with real time, this cannot be observed from the one-time correlation function alone. Non-equilibrium dynamics can occur for a variety of reasons, including aging, relaxation and rejuvenation processes. For non-equilibrium dynamics, it is important to use a *two-time correlation function* $\left(C(q, t_1, t_2)\right)$ which maps all possible combinations of time delay and plot the behavior through real time. This is described using the function below,

$$C(q, t_1, t_2) = \frac{\langle I(q, t_1) I(q, t_2) \rangle}{\langle I(q, t_1) \rangle \langle I(q, t_2) \rangle}$$

where intensity is correlated between pixels at two specific times, t_1 and t_2. This is done for every combination of time points and mapped out like shown in Fig. 2.18. The highest intensity of correlation will occur across the diagonal (shown as a yellow line) as at this point, $t_1 = t_2$. Following the blue and green arrows outwards the intensity drops as $|t_1 - t_2|$ increases. The arrows indicate a singular one-time correlation curve for a certain wait time. The correlation as plotted in Fig. 2.16 and Fig. 2.17, is an average of all possible individual one-time correlation function, while the two-time correlation function shows every possible correlation in time.

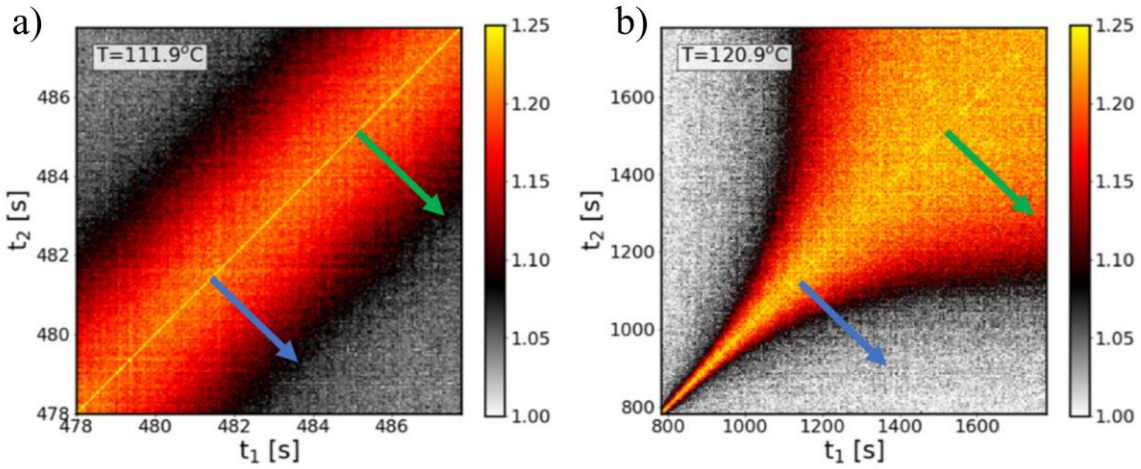

*Figure 2.18: Two-time correlation maps where **(a)** indicates a sample in equilibrium while **(b)** shows a sample that has aging. Blue and green arrows indicate examples of individual one-time correlation curves [29].*

In Fig. 2.18(a), the width of the bright diagonal stays relatively constant, indicating that the behavior is relatively constant with real time. However, in Fig. 2.18(b), the width of the diagonal drastically changes which is indicative of non-equilibrium behavior.

2.5: Summary

This chapter provides background for the sample and experimental methods used for the research in this thesis including pulsed laser deposition, x-ray scattering, and XPCS. Experimental conditions were outlined as XPCS was conducted on an 80 nm $BaTiO_3$ thin film at the CHX beamline in the NSLS-II. Additionally, data analysis methods such as the one-time and two-time correlation functions were introduced. Next, Chapter 3 will discuss results from XPCS and analysis using correlation functions with. Chapter 4 will conclude with a summary and future outlooks.

Chapter 3: XPCS study of *a*/*b* domain fluctuations in $BaTiO_3$

In this chapter, I present the findings from x-ray photon correlation spectroscopy (XPCS) measurements used to capture the temporal and spatial fluctuations of ferroelectric domains in $BaTiO_3$ films. The sample was characterized using x-ray diffraction (XRD) and piezoelectric force microscopy (PFM) prior to synchrotron experiments. Subsequently, I present the XPCS results, including the determination of decay constants for the correlation functions. Furthermore, trends in q-space are examined by analyzing fluctuations between higher-order peaks and considering q-dependent regions of interest (ROIs) within a peak. Our measurements reveal a strong temperature dependence in the fluctuation dynamics, along with potential evidence of q-dependence.

3.1 Preliminary characterization

The sample used for XPCS measurements is a $BaTiO_3$ thin film grown on an $NdScO_3$ substrate, with a $SrRuO_3$ bottom electrode. The sample is prepared by our collaborators Dr. A.S. Everhardt and Dr. S. Matzen. They performed structural characterization using XRD, PFM, and reciprocal space mapping (RSM). The x-ray diffraction pattern of the $BaTiO_3$ (001) peak is presented in Fig. 3.1. The $BaTiO_3$ and $NdScO_3$ Bragg peaks overlap due to their similar lattice parameters, with a small $SrRuO_3$ peak visible to the high angle side of the $BaTiO_3$/ $NdScO_3$ Bragg peak. Thicknesses of each layer were calculated by fitting Kiessig fringes, which are finite size oscillations that arise due to constructive and destructive interference between two interfaces.

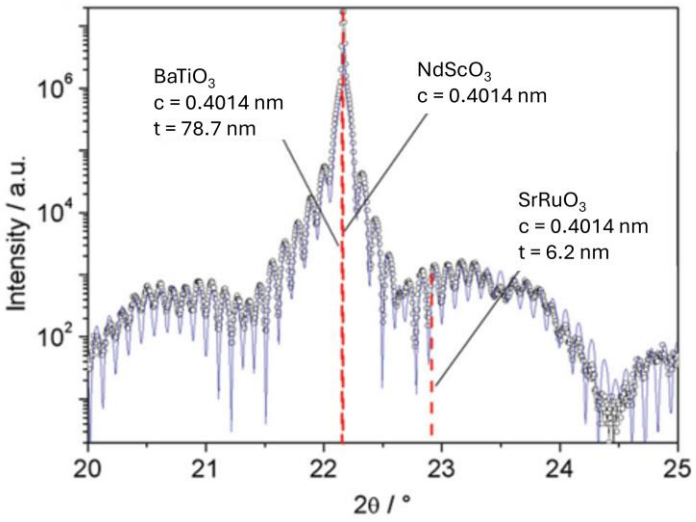

Figure 3.1: X-ray diffraction of $BaTiO_3$ thin film with $NdScO_3$ substrate peak, and $SrRuO_3$ peak where black dots are data points, and the blue line is the fit of oscillations [13].

To confirm ferroelectric domain patterns below and above the transition temperature $T_R \sim 55°C$, our collaborators performed lateral piezoelectric force microscopy (lateral PFM) at 25°C and 70°C. In lateral PFM, variation in polarization directions produces contrast in the image, as shown in Fig. 3.2. At 25°C, the domains show ordering along the *a* and *b* crystallographic directions, while at 70°C, the domains transition to *a*/*c* orientation.

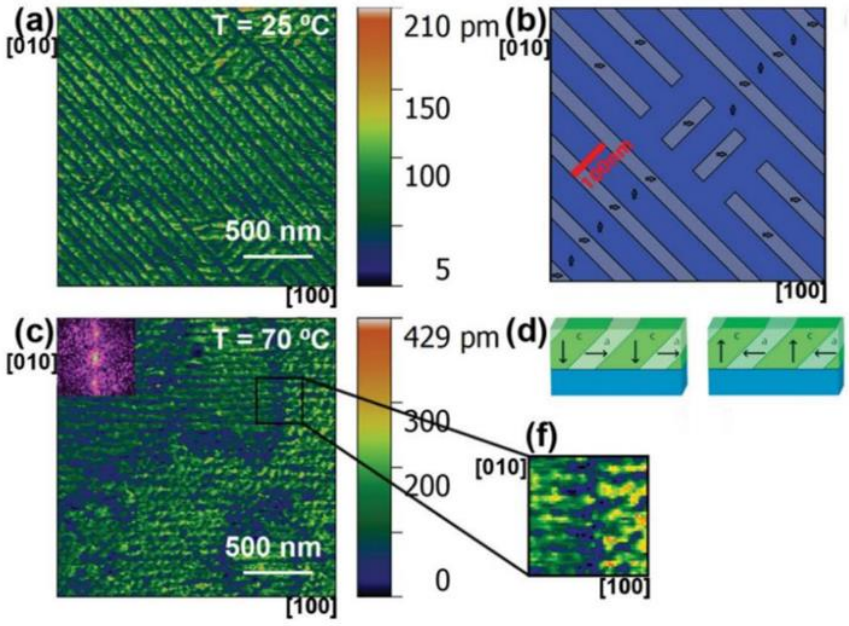

Figure 3.2: PFM images of $BaTiO_3$ domain structure. (a) 25°C shows a/b domain ordering, (c) 70°C shows a/c domain ordering, (b) schematic of a/b domains, and (d) schematic of a/c domains, (f) zoomed in view of domain morphology showing "zig-zag" pattern [13].

Since the polarization of *a*/*b* domains lie in plane, we accessed an in-plane peak to observe scattering contributions. Considering beamline constraints and the need to optimize peak intensity, the (103) Bragg peak was selected. To verify the presence of domain scattering at the (103) peak before conducting XPCS measurements at synchrotron, RSMs were collected at room temperature revealing intensity modulations from domains, as shown in Fig. 3.3.

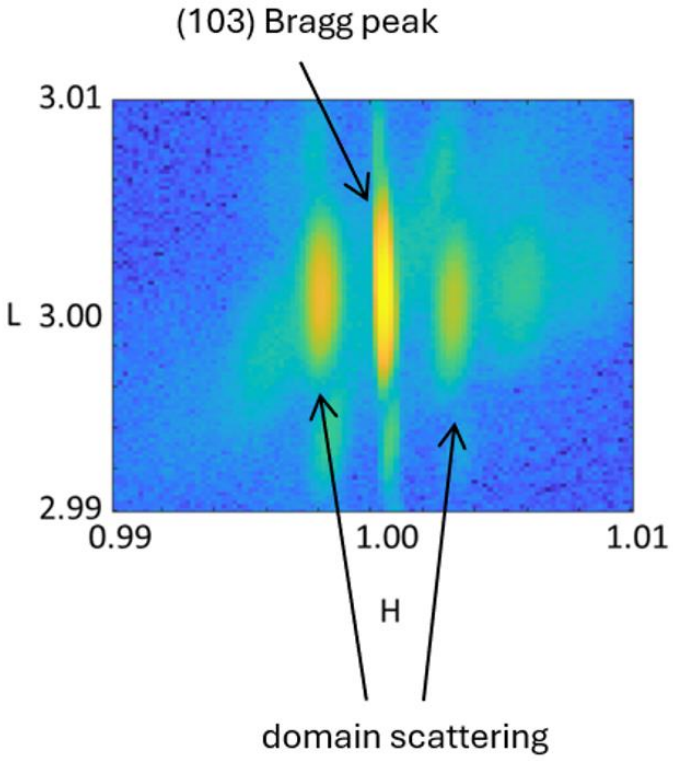

Figure 3.3: RSM of $BaTiO_3$ film (103) peak measured using Bruker D8 Diffractometer with Cu K_α x-rays.

3.2 Measurements of *a*/*b* domains in $BaTiO_3$

To measure fluctuations of *a*/*b* domains, XPCS measurements were conducted at the Coherent Hard X-ray scattering (CHX) beamline in the National Synchrotron Light Source II (NSLS-II) in Brookhaven National Laboratory (BNL). A series of scans were performed at temperatures 35°C to 65°C in 5°C increments, resulting in a total of seven scans. To ensure thermal equilibrium, each temperature was stabilized for one hour before starting the XPCS measurement. Each scan is three hours long with one image taken every second, yielding a total of 10,800 images total per scan. The scattered beam was collected by a two-dimensional Eiger X 1M detector positioned 1.5 m from the sample. Due to the highly coherent x-rays, scattered light undergoes constructive and destructive interference, specific to local heterogeneities in the sample, resulting in a *speckle* pattern. An average detector image and example speckle patterns are shown in Fig. 3.4. A notable

aspect of this experiment was the ability to access to higher orders of scattering peaks due to the use of a two-dimensional detector. Each peak was analyzed individually and will be discussed in the following sections.

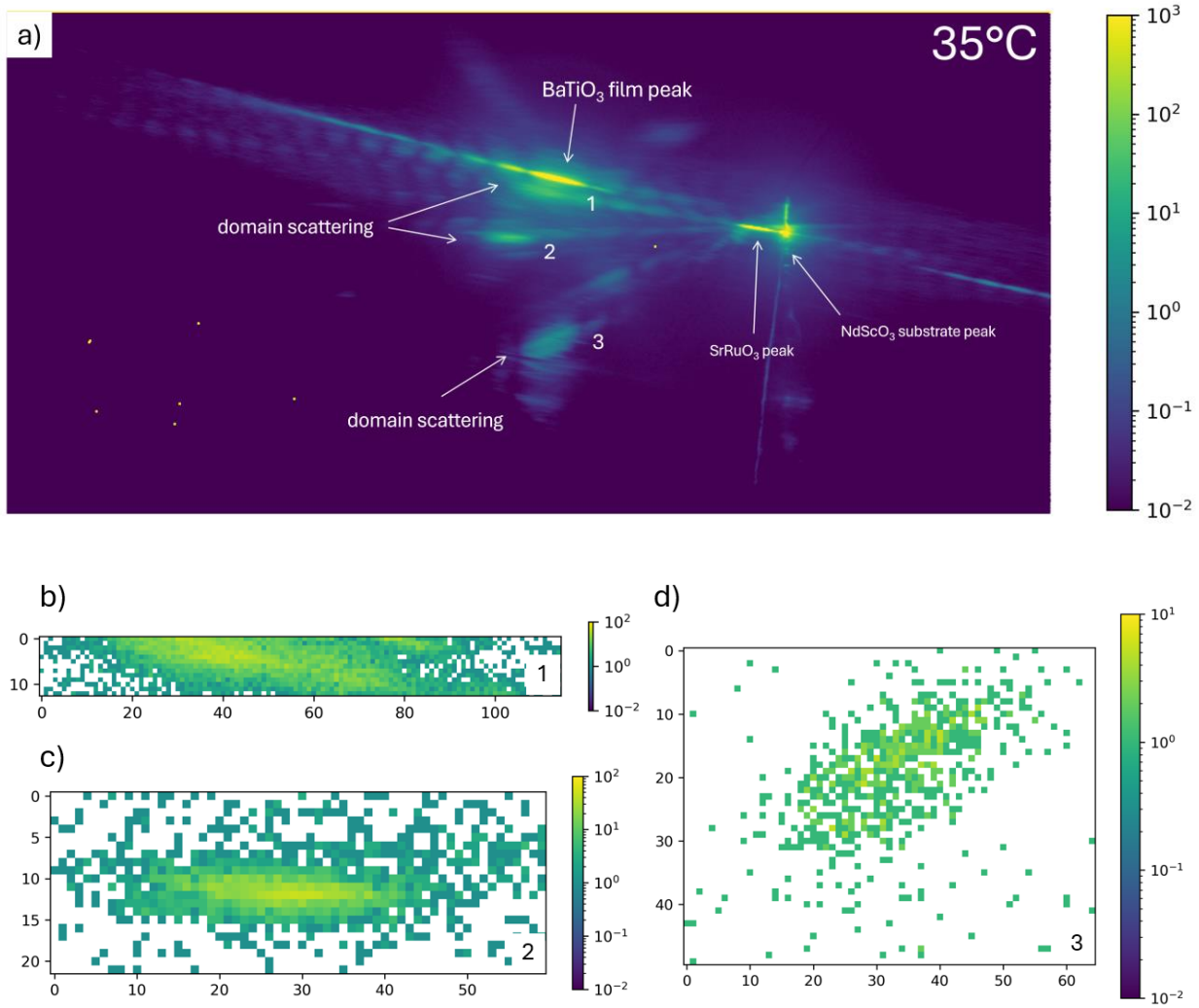

Figure 3.4: (a) Averaged diffraction pattern of (103) peak at 35°C. Speckle patterns from a single detector image shown for (b) ROI 1, (c) ROI 2, and (d) ROI 3. The average image in (a) represents average seen in 3-hour XCPS.

To perform auto-correlation functions, it is essential to select specific regions of interest (ROIs) on the detector to ensure that the contributions of each scattering peak are analyzed separately.

Defining ROIs is also crucial for excluding background noise or extraneous pixels that could artificially influence the correlation plots. Several methods exist for establishing ROIs. In this thesis, the peaks were fitted with a two-dimensional Gaussian function, and elliptical ROIs were defined based on the contours of the fit. This approach is effective in aligning the ROIs with the intensity distribution of the peaks. Each scattering peak is associated with an elliptical ROI, as illustrated in Fig. 3.5. In this thesis, the scattering peaks will be referred to as ROI 1, ROI 2, and ROI 3, corresponding to their labels in Fig. 3.4 and Fig. 3.5.

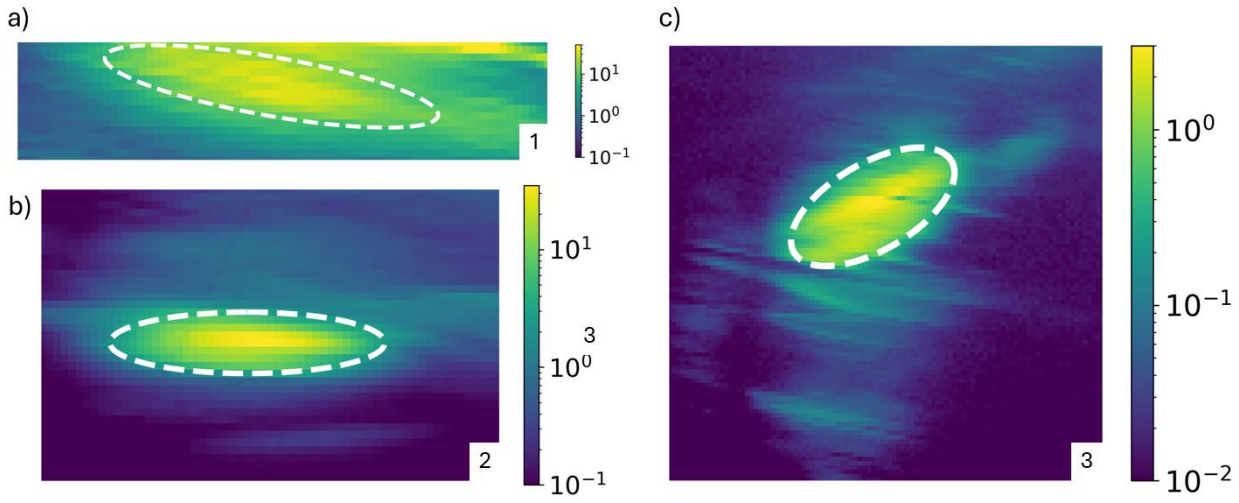

Fig 3.5: Elliptical ROI chosen for each peak – referred to as (a) ROI 1, (b) ROI 2 and (c) ROI 3.

3.3 Temperature dependence of *a*/*b* domains

The temperature-dependent evolution of each ROI was investigated by calculating integrated intensity, peak position shift, and full width at half maximum (FWHM) as a function of temperature. The parameters of each ROI were extracted by fitting the data with a two-dimensional gaussian function, the results are presented in Fig. 3.6.

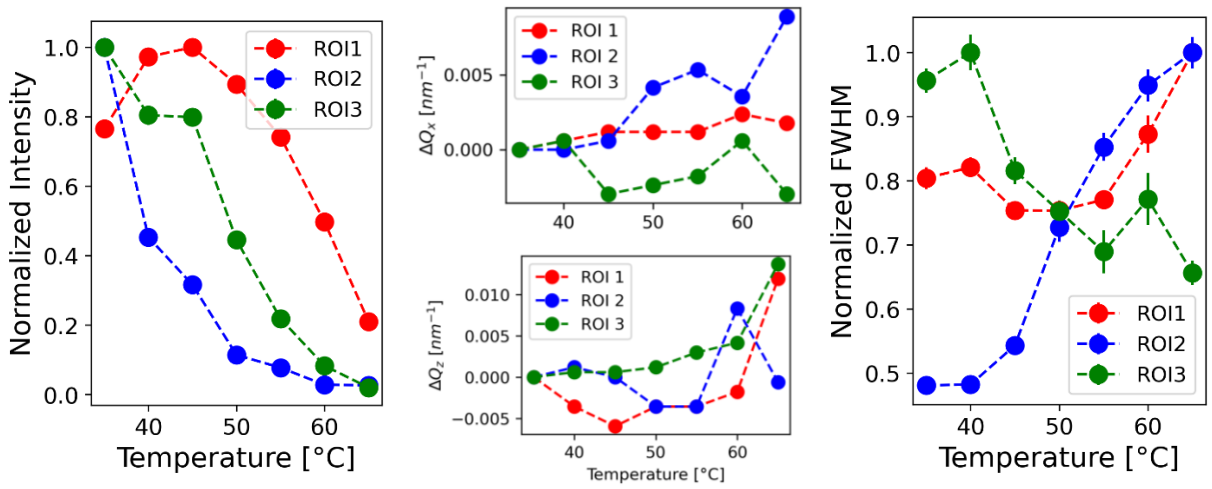

Figure 3.6: Normalized integrated intensity, peak shift in Q_x and Q_z, and normalized FWHM as a function of temperature for a/b domain scattering in ROI 1, 2, and 3.

The normalized intensity of each ROI exhibited a decreasing trend with increasing temperature. This observation aligned with the expectation that *a*/*b* domains reorient into *a*/*c* domains near the transition temperature $T_R \approx 55°C$. Notably, no significant trend was observed in the shift of peak position; all three ROIs maintain a relatively constant peak position, with some variability at elevated temperatures likely attributed to the lower intensity of domain scattering. Regarding FWHM, both ROI 1 and ROI 2 exhibit an increase with higher temperature, suggesting an increase in disorder within the system. In contrast, ROI 3 displayed a decrease in FWHM with increasing temperature. This trend could be due to textured features within the peak, as shown by the streaking observed in Figure 3.5c, which persists across changes in temperature can influence the FWHM. Further investigations are required to understand the underlying mechanisms contributing to the observed texture within the peak.

3.4 Correlation function analysis of *a*/*b* of domain fluctuations

As discussed above, XPCS scans were measured for three hours to capture the speckle pattern as a function of time. Next, speckle patterns were analyzed using the one-time correlation function (g_2) as discussed in Chapter 2.4.4. The g_2 for all three ROIs is plotted in Fig. 3.7. The intermediate scattering function (ISF) was then obtained from the g_2 as described in Chapter 2.4.4 and is plotted in Fig. 3.7.

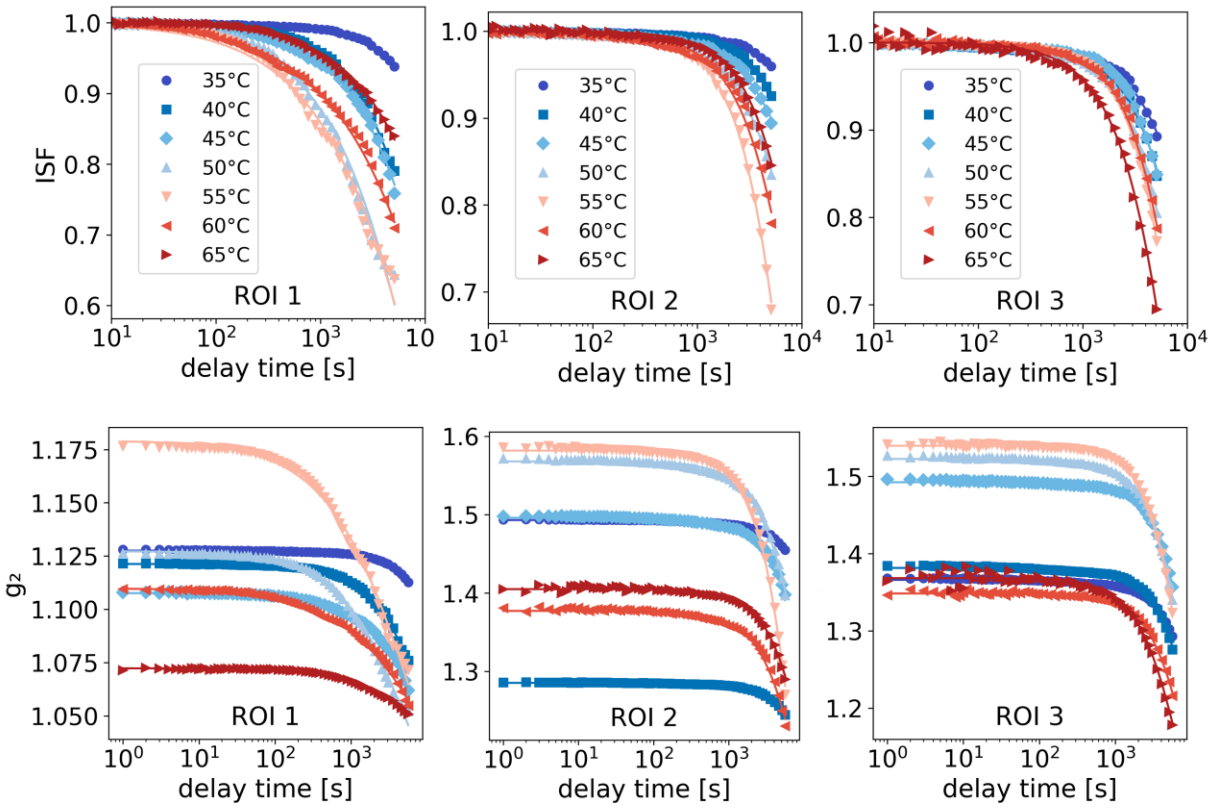

Figure 3.7: One-time correlation function (g_2) and intermediate scattering function (ISF) plotted as a function of temperature for ROI 1, 2, and 3. The dots represent data points while the solid line represents the exponential fit of the data.

For all three ROIs, the ISF demonstrated a pronounced temperature dependence. The sharp decay of ISF at higher temperatures showed that domain dynamics accelerates as the system approaches

the reorientation transition ($T_R \approx 55°C$). For ROI 1 and ROI 2, the fastest timescales are observed at 55°C, whereas for ROI timescales increase monotonously until 65°C. The ISF was fit using the exponential function: $\exp\left(-\frac{t}{\tau}\right)^{\beta}$. The decay constant ($\tau$), stretching exponent ($\beta$), and contrast factor ($A$) fit from g_2, are provided in Fig. 3.8 for all three ROIs.

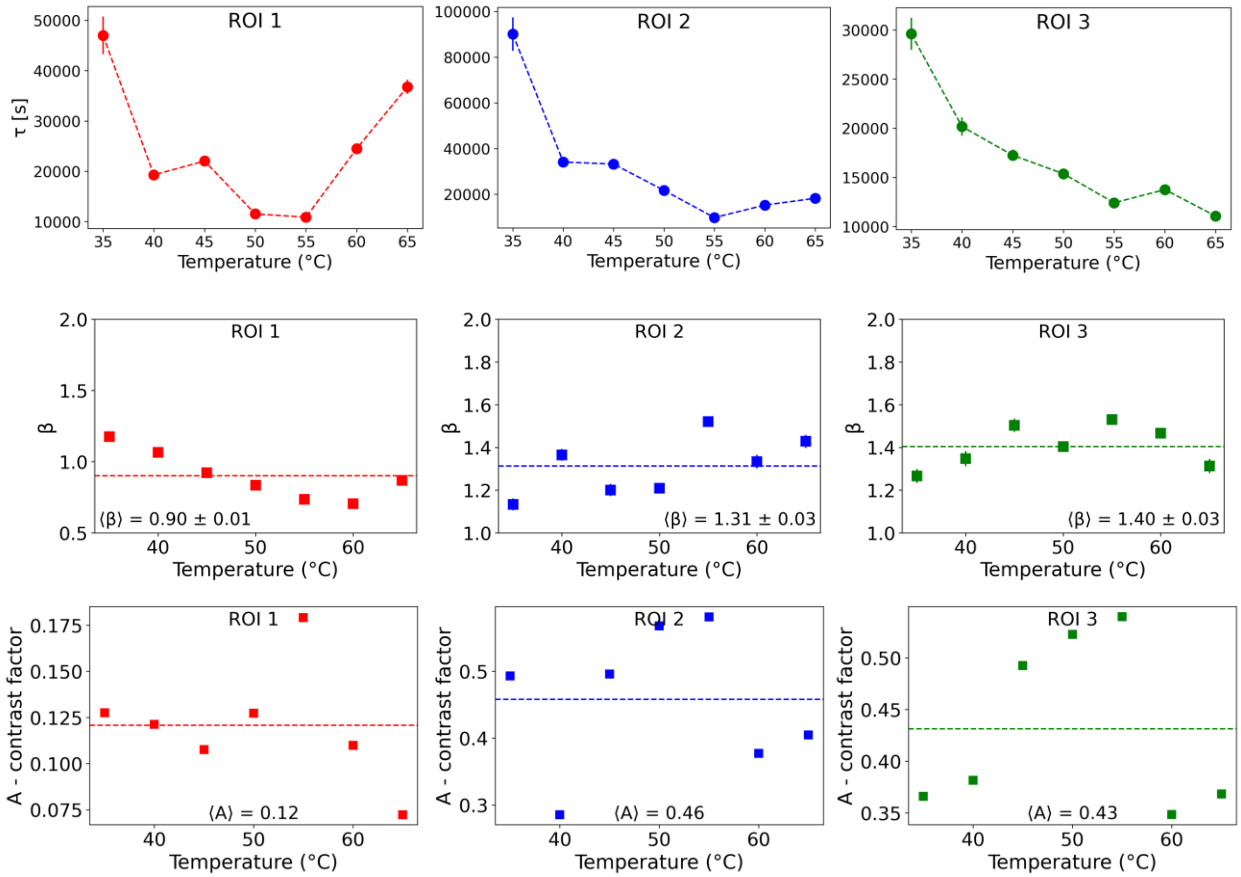

Figure 3.8: Decay constant (τ), stretching exponent (β), and contrast factor (A) as a function of temperature for ROI 1, 2, and 3. The dashed lines for β and A indicate the average value.

As mentioned previously, the decay constant (τ) measures how fast the material system decorrelates. Examining τ constants for each ROI, as shown in Fig. 3.8, τ decreases as the $T_R \approx$ 55°C is approached. This decrease indicated that the rate of fluctuations accelerates as temperature nears T_R. After reaching T_R, τ increases at 60°C for each ROI 1, indicating that fluctuations slow

down or stabilize slightly after the transition. However, no such increase is seen for ROI 2 and 3 where τ varies between 55°C and 65°C. The stretching exponent (β) and contrast factor (A) parameters, obtained from fits to ISF for each ROI, are also compared in Figure 3.11. The average β for ROI 1, 2, and 3 is 0.9 ± 0.01, 1.31 ± 0.03, and 1.4 ± 0.03 respectively. For ROI 2 and 3, β values exceed 1, which is indicative of jamming transition of fluctuation dynamics between *a*/*b* and *a*/*c* domain configurations. Jammed transitions occur as local displacements that produce long-range disorder due to relaxation from internal stress field. Stretching exponents where $\beta > 1$ were also observed in Li *et al.* for $BaTiO_3$ *a*/*c* domains and Zhang *et al.* for $PbTiO_3/SrTiO_3$ superlattice stripe domains. However, ROI 1 shows $\beta < 1$, which is indicative of liquid-like diffusive motion of atoms and molecules, commonly present in highly viscous liquids [30]. The observation of $\beta < 1$ for ROI 1 is surprising and could indicate that the peak originates from a different part of the sample, although simulations are required to confirm this. The contrast factor was independent of temperature and relies on external factors such as beamline coherence and sample parameters. There is no clear trend observed for contrast, which is similar to observations from previous experiments. Note that contrast of *a*/*b* domains was higher than those reported for *a*/*c* domains. This could be due to differences in beamline configurations between the two experimental studies.

3.4.1 Arrhenius fit to decay constants

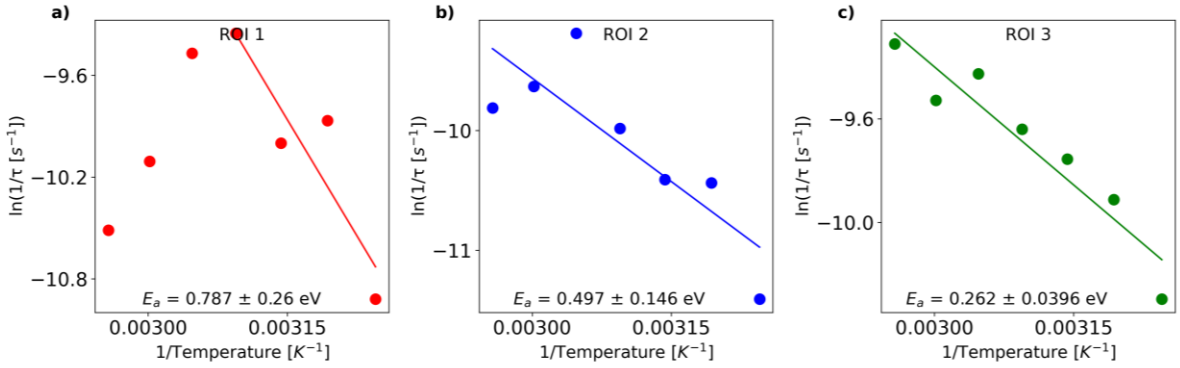

Figure 3.9: Plots of ln(1/τ) versus inverse temperature for (a) ROI 1, (b) ROI 2, (c) ROI 3 with linear fits to estimate an Arrhenius dependence. Estimated activation energies from linear fit (E_a) are reported.

Arrhenius fits to τ were performed to estimate the activation energies for thermal fluctuations, as shown in Figure 3.9. Note that for ROI 1 (in Figure 3.9a), the two highest temperature points are excluded, as the large increase in τ is not consistent with behavior where fluctuations are expected to increase with time. The activation energies for each ROI were found to be 0.787 ± 0.26 eV, 0.497 ± 0.146 eV, and 0.262 ± 0.0396 eV, respectively. The goodness of fit for each ROI can be assessed using the R^2 values, which are 0.82, 0.69, and 0.90 for ROI 1, 2, and 3, respectively, indicating moderate to strong relationships with the data.

These values are notably lower than the activation energies associated with domain pinning sites, such as the migration of oxygen vacancies, which has an activation energy of approximately 0.8 eV and is a well-documented mechanism for domain wall pinning. Activation energies for similar systems, such as *a*/*c* domains in $BaTiO_3$ and $PbTiO_3$/$SrTiO_3$ stripe domains, are estimated to be approximately 0.67 ± 0.27 eV and 0.35 ± 0.21 eV, respectively. It was proposed for both kinds of domain fluctuations may be promoted through the generation and annihilation of topological defects, which could similarly influence the behavior of *a*/*c* domains [15-16].

3.5 Comparison of *a*/*b* and *a*/*c* domains

Decay constant fluctuations of *a*/*b* domain constants were compared with decay constants of fluctuations measured by Li *et al.* for *a*/*c* domains. Values have been extracted from Li *et al*. and replotted in the following figures.

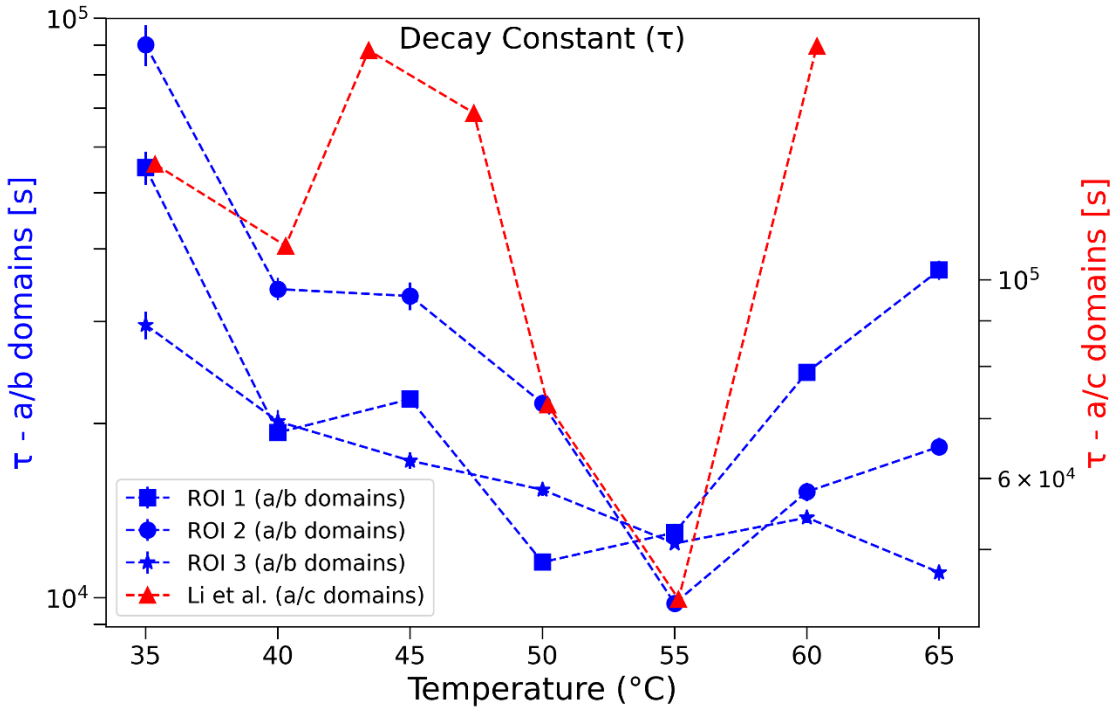

Figure 3.10: Decay constant (τ) as a function of temperature for each ROI from a/b *domain scattering overlayed with* a/c *domain scattering extracted from Li et al* [16].

In Fig. 3.10, the values as well as temperature dependence of τ are very similar for both *a*/*b* and *a*/*c* domains. This indicates that fluctuations of both *a*/*b* and *a*/*c* domains occur and lead to domain orientation transitions.

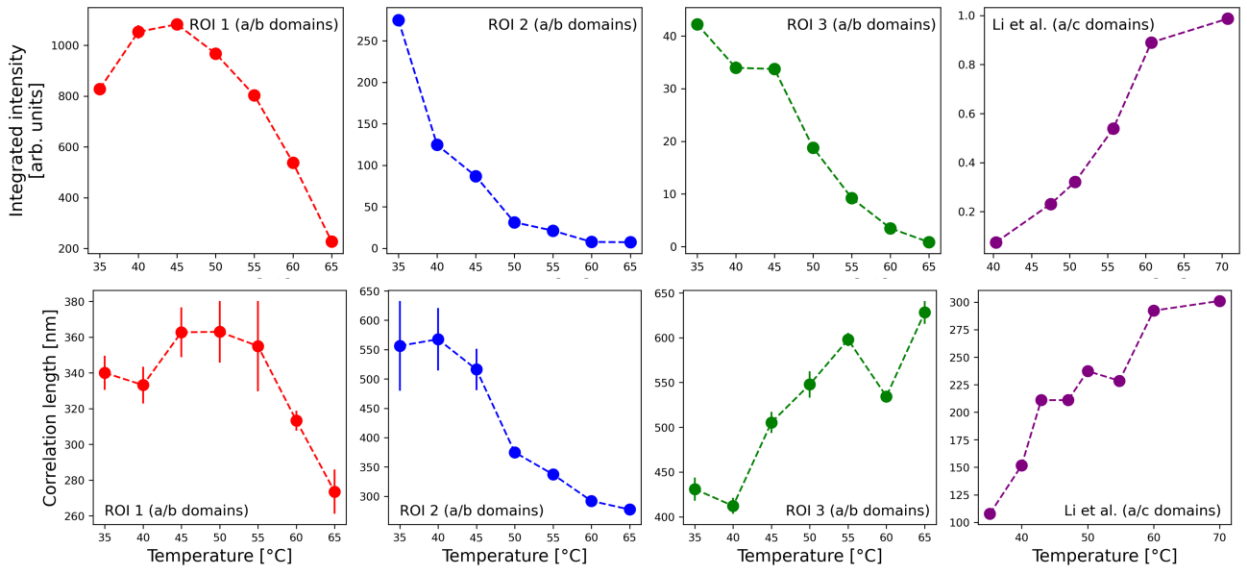

Figure 3.11: (Top) Integrated intensity plotted as a function of temperature for a/b domains in ROI 1, 2, and 3 and a/c domains found in Li et al. (Bottom) Correlation length obtained from FWHM is also plotted for ROI 1, 2, 3 and a/c domain peak in Li et al. [16].

Fig. 3.11 presents a comparative analysis of the temperature-dependent trends in integrated intensity and correlation length (λ) between *a*/*b* and *a*/*c* domains. The integrated intensity displays opposing behaviors between these domain types, a trend that is consistent with the expected reconfiguration of *a*/*b* domains into *a*/*c* domains around the transition temperature (T_R), leading to a reduction in the intensity of *a*/*b* peaks. Correlation length (λ), defined as $\lambda = \frac{2\pi}{\mathrm{FWHM}}$, serves as a physical measure of the extent of order within the system, with larger correlation lengths indicating higher order. In the case of *a*/*b* domains, the correlation length within ROI 1 and ROI 2 decreases as the temperature nears T_R, suggesting increased disorder at elevated temperatures which is expected as *a*/*b* domains disappear, and *a*/*c* domains appear. This observation is consistent with increase in correlation length for *a*/*c* domains too. The only exception is ROI 3 which may be attributed to texture effects within the scattering peak, as previously discussed.

3.5.1 Non-equilibrium behavior

Two-time correlation analysis, as shown in Fig. 3.12, also pointed towards non-equilibrium fluctuation dynamics.

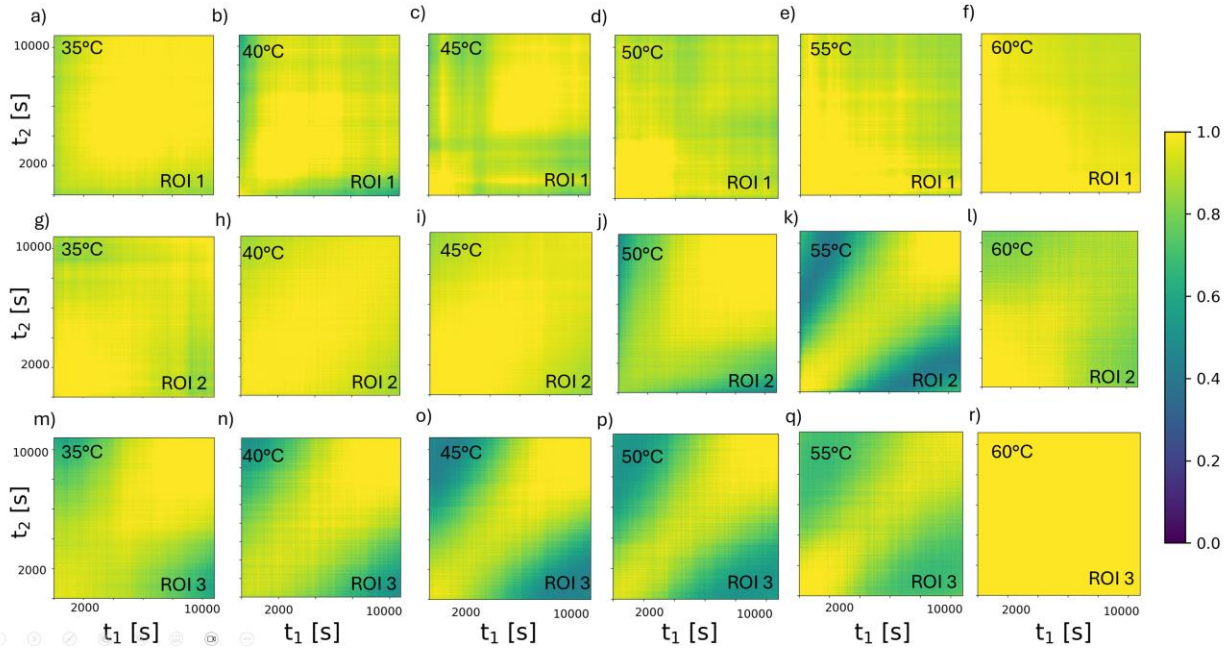

Figure 3.12: Two-time correlation plots for ROI 1, 2, and 3 as a function of temperature in a/b domains.

While Li *et al*. did not observe evidence of non-equilibrium dynamics, there is clear evidence of such behavior in *a*/*b* domains. Non-equilibrium dynamics, such as aging, occurs when the critical behavior of a sample changes as a function of real time. This could be due to a speeding up or slowing down of fluctuations over real time in order to reach a static state. Figure 3.12b and Fig. 3.12m are a few examples where the width of the center diagonal is not constant, indicating that fluctuations vary throughout real-time and suggesting the system could be aging. This could be due to experimental configurations but may also indicate differences between dynamics of *a*/*b* and *a*/*c* domains. The origination of non-equilibrium dynamics in *a*/*b* domains is still not known and further studies are required to establish a deeper understanding.

3.6 *Q*-dependence

Finally, I compare the *q*-dependence within an individual peak to identify potential trends across in the width of a scattering peak. The width of a scattering peak can be influenced by factors such as strain, crystallite size, and disorder due to defects like domain walls. Analyzing distinct rings in *q*- space within a peak can provide detailed insights into scattering from different components of the domain configuration, such as domains versus domain walls. The *q*-dependent analysis will focus primarily on ROI 3, as it is the largest peak in terms of pixels on the detector, with a validation test conducted on ROI 2.

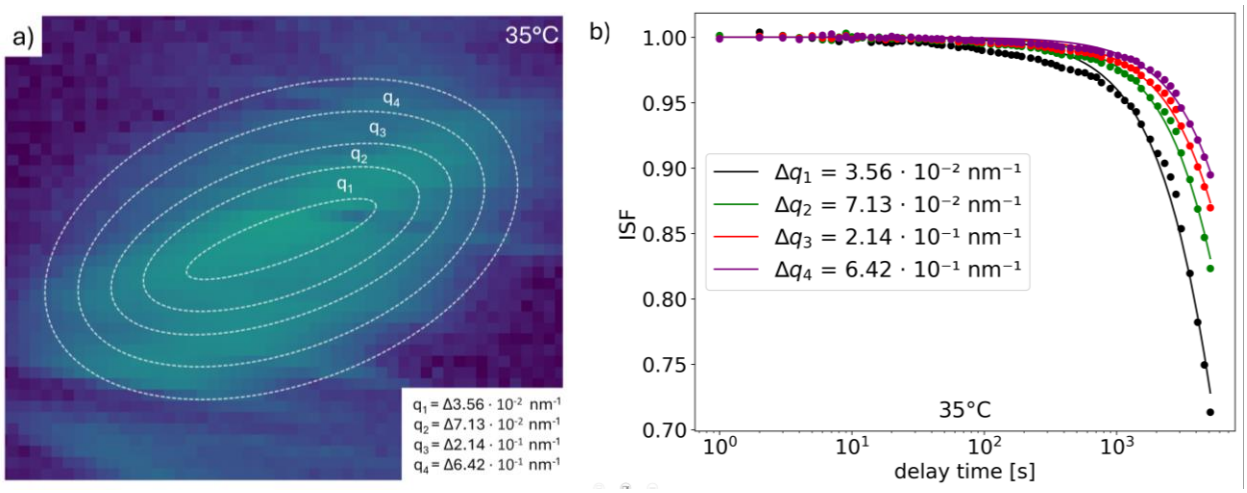

Fig 3.13: (a) Schematic of hollow q-rings with ellipses as the boundaries of each ring for ROI 3 at 35°C, displacement from center ring is shown in legend. (b) ISF of each q-ring at 35°C.

Four rings of equal width each progressively larger, were defined as shown in Fig. 3.13a. The width of each ring was six pixels, with specific displacements in inverse nanometers (nm^{-1}) detailed in the legend. One-time correlation function and ISF were calculated for all four *q*-rings at each temperature. An example of the ISF for 35°C is shown in Figure 3.13b. Here, the fluctuations slow down with increasing distance from the center of the peak, as indicated by the

smallest drop in ISF for q_4 and the largest drop for q_1. This trend is further quantified using the exponential fits of each ISF, as plotted in Fig. 3.14.

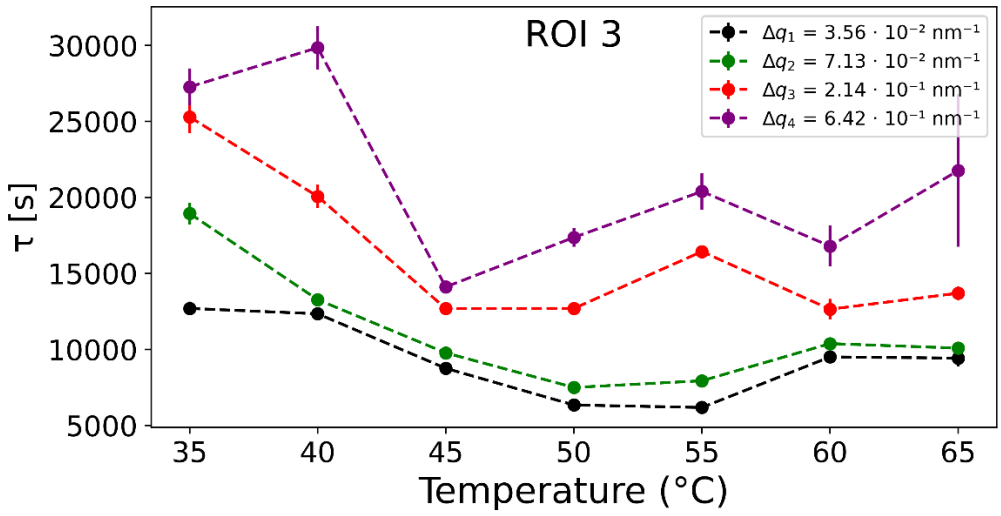

Figure 3.14: τ – decay constant fits for each q-ring as a function of temperature.

Fig. 3.12 demonstrates that the trend of fluctuations slowing down with increasing q is valid for every temperature between 35°C to 65°C. For each temperature, the smallest decay constants are seen for q_1 with values progressively increasing for q_2, q_3, and q_4. The largest τ at q_4 suggests that the outer regions of the peak experience the slowest fluctuations. According to Porod's law, the tails of domain scattering peaks originate from domain walls, as breadth of the peak is directly related to the domain wall area per unit volume [31]. A decrease in fluctuations at the outskirts of the scattering peak may indicate that domain walls remain more rigid while the local domains continue to fluctuate. To directly examine this trend, τ as a function of q-ring for each temperature is plotted in Fig. 3.15.

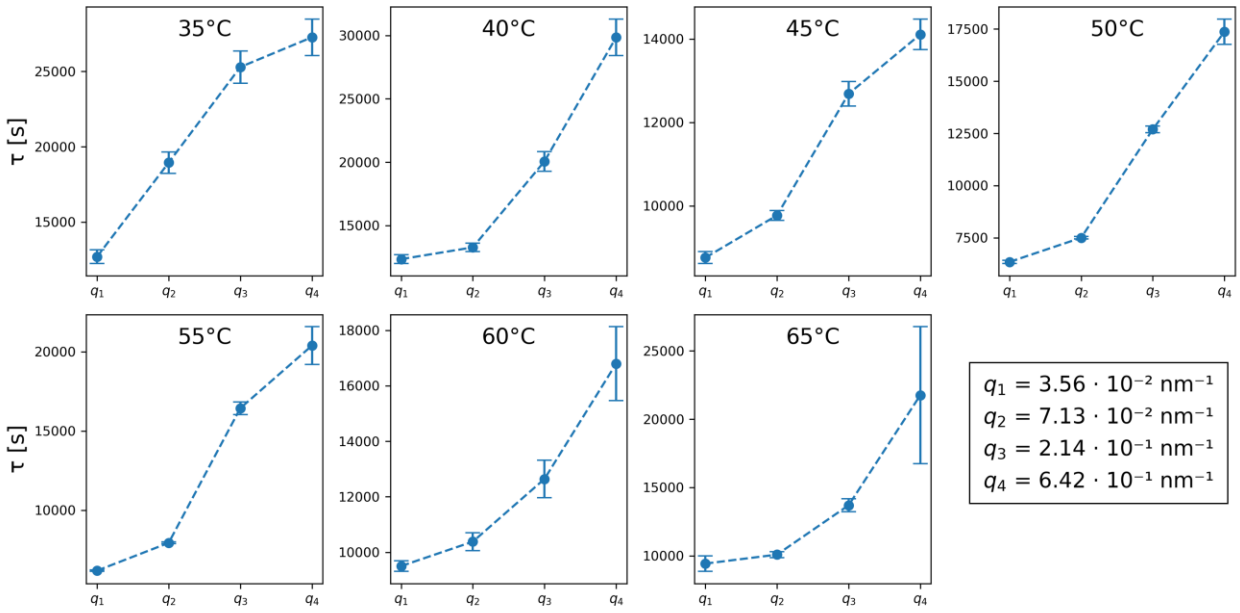

Figure 3.15: Decay constant fits as a function of q for each temperature in ROI 3.

Fig. 3.15 shows an increase in τ as a function of increasing q-space for each temperature, with 35°C to 55°C exhibiting a linear increase and 35°C to 65°C exhibiting quadratic increase. The fluctuation slowdown could be related to the differences in dynamics between domains and domain walls and relate to possible driving mechanisms for domain reconfiguration from *a*/*b* to *a*/*c* domains. One possible explanation is that domains reconfigure through long-range reorientations, while local regions remain stable or pinned by domain walls.

Although the scattering peaks in ROI 1 and ROI 2 do not contain enough pixels for a thorough q-dependent analysis, a validation was performed to check whether the slowdown also occurs in other scattering peaks. For ROI 2, the peak was divided into two halves (q_1 and q_2) and the dynamics between these regions were compared across temperatures. Despite some outliers in the temperature dependent trends due to the lower SNR, there is evidence that the q_2 region exhibits slower dynamics than the q_1 region, as shown in Fig. 3.16. The decay constants at each temperature

for q_2 are larger than those for q_1, validates the findings from ROI 3 that the tails of the peak, likely originating from domain wall scattering, fluctuate more slowly than the center of the peak.

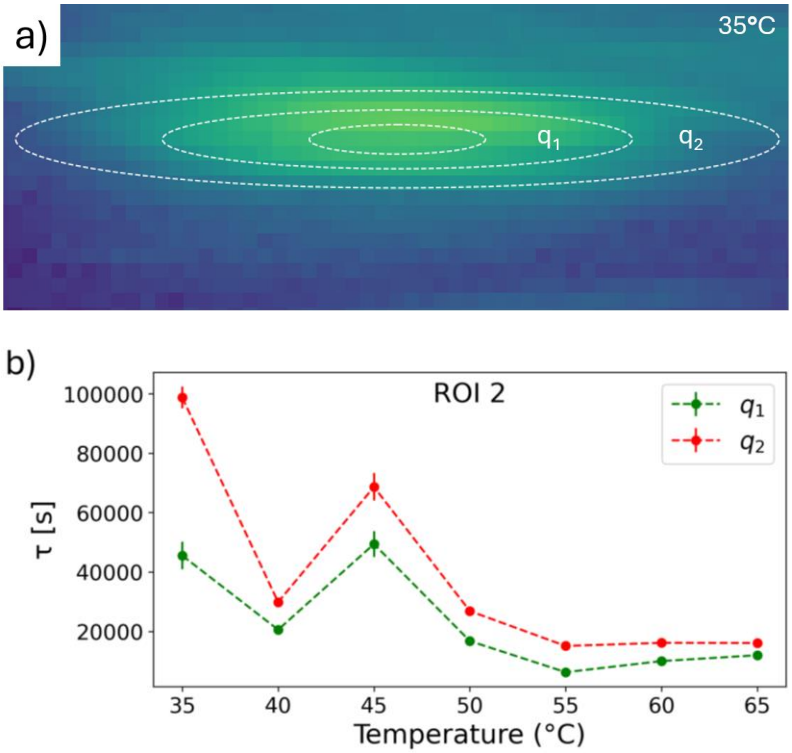

Figure 3.16: (a) Schematic of q_1 and q_2 with ellipses as the boundaries of each ring for ROI 2 at 35°C (b) decay constant fits as a function of temperature for q_1 and q_2 in ROI 2.

3.7 Summary

This chapter explores the temperature dependent behavior and fluctuation dynamics of *a*/*b* domains. XPCS results show that *a*/*b* domains exhibit behavior consistent with *a*/*c* domains studied by Li *et al*. The decay constants and FWHMs for *a*/*b* domains display similar trends to those observed in a/c domains. Notably, the opposing trend in integrated intensity, with *a*/*b* domains weakening as temperature increases, aligns with the expected transformation around T_R ≈ 55°C. Additionally, the stretching exponent (β) values for *a*/*b* domains fall within the range observed for *a*/*c* domains, with a few outliers, further supporting the similarity in reorientation

mechanisms between the two domain types. Further analysis of the *a*/*b* domains across different ROIs reveals variations that reflect distinct aspects of the domain dynamics. While decay constants show a consistent trend of decreasing until $T_R \approx 55°C$, evidence of non-equilibrium behavior across ROIs suggest complex dynamics at play. *Q*-dependent analysis indicates that domain walls fluctuate slower than the domains themselves, providing insights into the dynamics of domain versus domain wall reconfiguration.

Chapter 4: Conclusion and future outlook

4.1 Conclusion

In this thesis, the fluctuation dynamics of ferroelectric domains in $BaTiO_3$ were investigated to better understand the potential driving mechanisms behind domain reconfigurations. The primary method employed x-ray photon correlation spectroscopy, a technique that maps temporal and spatial fluctuations in intensity of speckle patterns to reveal dynamics of a system. The sample studied was an 80 nm $BaTiO_3$ thin film on a $NdScO_3$ substrate with a 6nm $SrRuO_3$ buffer layer, known to undergo a transition from *a*/*b* to *a*/*c* domain configuration (T_R) near 55°C to minimize system energy. This thesis explores the dynamics of *a*/*b* domains in order to understand the landscape of domain configurations in $BaTiO_3$.

Initially, I compared the behavior of *a*/*b* domains with previously studied *a*/*c* domains in $BaTiO_3$. Similar trends in timescales and stretching exponents suggest that there may be coupled driving mechanisms for reorientation in both *a*/*b* and *a*/*c* domains. However, and evidence of non-equilibrium dynamics suggest distinct aspects in each domain reconfiguration. The subsequent aim focused on comparing different regions within *q*-space for *a*/*b* domains. First, I analyzed the dynamics across higher-order scattering peaks observed in the experiment. While there were similar trends in timescales and peak intensities, distinct behavior was noted in the peak widths of higher-order peaks. To further explore *q*-space dependence, I conducted a *q*-dependent analysis within a specific scattering peak. This revealed that fluctuation timescales slowed as the analysis extended to tails of scattering peaks. Considering that the tails of scattering peaks are attributed to smaller defects such as domain walls, this suggests that domain walls fluctuate more slowly than

the entire domain. This insight could enhance our understanding of how domains fluctuate during reorientation into new configurations.

4.2 Future outlooks

In this section, I outline potential future directions to build upon the research presented in this thesis. First, I propose investigating the role of strain in domain landscapes and exploring how tuning misfit strain in thin films could enable access to a broader range of domain configurations. For the $BaTiO_3$ sample studied here, two primary domain configurations are accessible (*a*/*b* and *a*/*c*) by using $NdScO_3$ as a substrate. While both configurations have been examined using XPCS, additional domain configurations can be achieved via epitaxial strain. This can be done using similar substrates in the scandate family such as $DyScO_3$ and $GdScO_3$, which have slightly smaller lattice parameters than $NdScO_3$. A valuable comparison would be to investigate whether different domain configurations in $BaTiO_3$ exhibit similar timescales and transition behaviors.

Furthermore, studies on domain fluctuation behavior in $BaTiO_3$ could be expanded to non-equilibrium techniques involving external stimuli. For example, applying an electric field could be used to tune domain polarization directions or induce domain switching, while optical excitation could reveal ultrafast dynamics. Although this thesis primarily explores driving mechanisms in equilibrium experiments over longer timescales, extending the research to faster timescales beyond the reach of XPCS could provide new insights. Optical excitation on ultrafast timescales may uncover novel behavioral trends, as the underlying process can occur on nano- or femtosecond scales.

References

[1] National Renewable Energy Laboratory, "Piezoelectric and Ferroelectric Materials Research," NREL, 2023.

[2] J. Als Nielsen and D. McMorrow, *Elements of Modern X-ray Physics*, 2nd ed., Wiley, 2011.

[3] R. Whatmore, *Ferroelectric Materials*, in *Electronic Properties of Engineering Materials*.

[4] Princeton University, "Perovskite Structure Tutorial," 2019.

[5] A. S. Everhardt, *Complete Thesis: Novel phases in ferroelectric $BaTiO_3$ thin films*, Ph.D. dissertation, Univ. of Groningen, Netherlands, 2017.

[6] P. Sharma et al., "Functional Ferroic Domain Walls for Nanoelectronics," 2019.

[7] Y. Nahas et al., “Inverse transition of labyrinthine domain patterns in ferroelectric thin films,” *Nature*, 2020.

[8] W. Cao, "Constructing Landau-Ginzburg-Devonshire Type Models for Ferroelectric Systems Based on Symmetry"

[9] A. L. Roytburd, S. P. Alpay, L. Bendersky, and R. Ramesh, "Three-Domain Architecture of Stress-Free Epitaxial Ferroelectric Thin Films," *Journal of Applied Physics*, vol. 90, no. 1, 2001.

[10] V. G. Koukhar et al., “Thermodynamic theory of epitaxial ferroelectric thin films with dense domain structures,” *Phys. Rev. B,* 2001.

[11] M. Y. Gureev et al., “‘Head-to-head’ and ‘tail-to-tail’ 180-degree domain walls in an isolated ferroelectric,” 2011.

[12] P. H. J. Koumoulos, M. Trompoukis, et al., "Sensors," vol. 10, no. 3, pp. 1935, 2010. doi: 10.3390/s100301935.

[13] A. S. Everhardt et. al., “Ferroelectric domain structures in Low-Strain $BaTiO_3$,” *Adv. Electronic Materials.,* 2015.

[14] A. S. Everhardt et al., “Periodicity-doubling cascades: Direct observation

in ferroelastic materials,” *Physical Review Letters*, 2019.

[15] Q. Zhang et al., “Thermal Fluctuations of Ferroelectric Nanodomains in a FerroelectricDielectric PbTiO3/SrTiO3 Superlattice,” *Phys. Rev. Lett.*, 2017.

[16] J. Li et al., “Domain fluctuations in a ferroelectric low-strain $BaTiO_3$ thin film,” *Phys. Rev. Materials*, 2020.

[17] J. Stöhr, *X-ray Interactions with Matter*, 1st ed., Springer, 1992.

[18] "Research Tutorial," ETH Zurich.

[19] M. Kotlarchyk, "Scattering Theory," in *Encyclopedia of Spectroscopy and Spectrometry*, 1st ed., Academic Press, 1999.

[20] "Bragg's Law," Wikipedia, The Free Encyclopedia.

[21] G. F. Harrington et. al., “Back-to-Basics tutorial: X-ray diffraction of thin films,” *Journal of Electroceramics*, 2021.

[22] P. Willmott, *An Introduction to Synchrotron Radiation: Techniques and Applications*. 1st ed. Oxford, UK: Oxford University Press, 2018.

[23] "Synchrotron Radiation," Wikipedia.

[24] G. Grübel, A. Madsen, and A. Robert, "X-Ray Photon Correlation Spectroscopy (XPCS)."

[25] N. Hua., “Discerning element and site-specific fluctuations of the charge-orbital order in Fe_3O_4 below the Verwey transition,” *Phys. Rev. Materials*, 2023.

[26] E. N. Glytsis, “Optical Engineering Prof. Elias N. Glytsis university of Athens spatial temporal coherence,” *School of Electrical and Computer Engineering – National Technical University of Athens*.

[27] L. Wiegart et al., “X-ray optical simulations supporting advanced commissioning of the coherent hard x-ray beamline at NSLS-II,” *Society of Photo-Optical Instrumentation Engineers*, 2017.

[28] A. Nogales et al., “X Ray Photon Correlation Spectroscopy for the study of polymer dynamics,” *European Polymer Journal*, 2016.

[29] R. Kukreja et al., “Orbital domain dynamics in magnetite below the verwey transition,” *Physical Review Letters*, 2018.

[30] L. Cipelletti et al., “Universal non-diffusive slow dynamics in aging soft matter,” *Faraday discussions*, 2003

[31] B. Guzelturk et al., “Sub-Nanosecond Reconfiguration of Ferroelectric Domains in Bismuth Ferrite,” *Advanced Materials*, 2023.